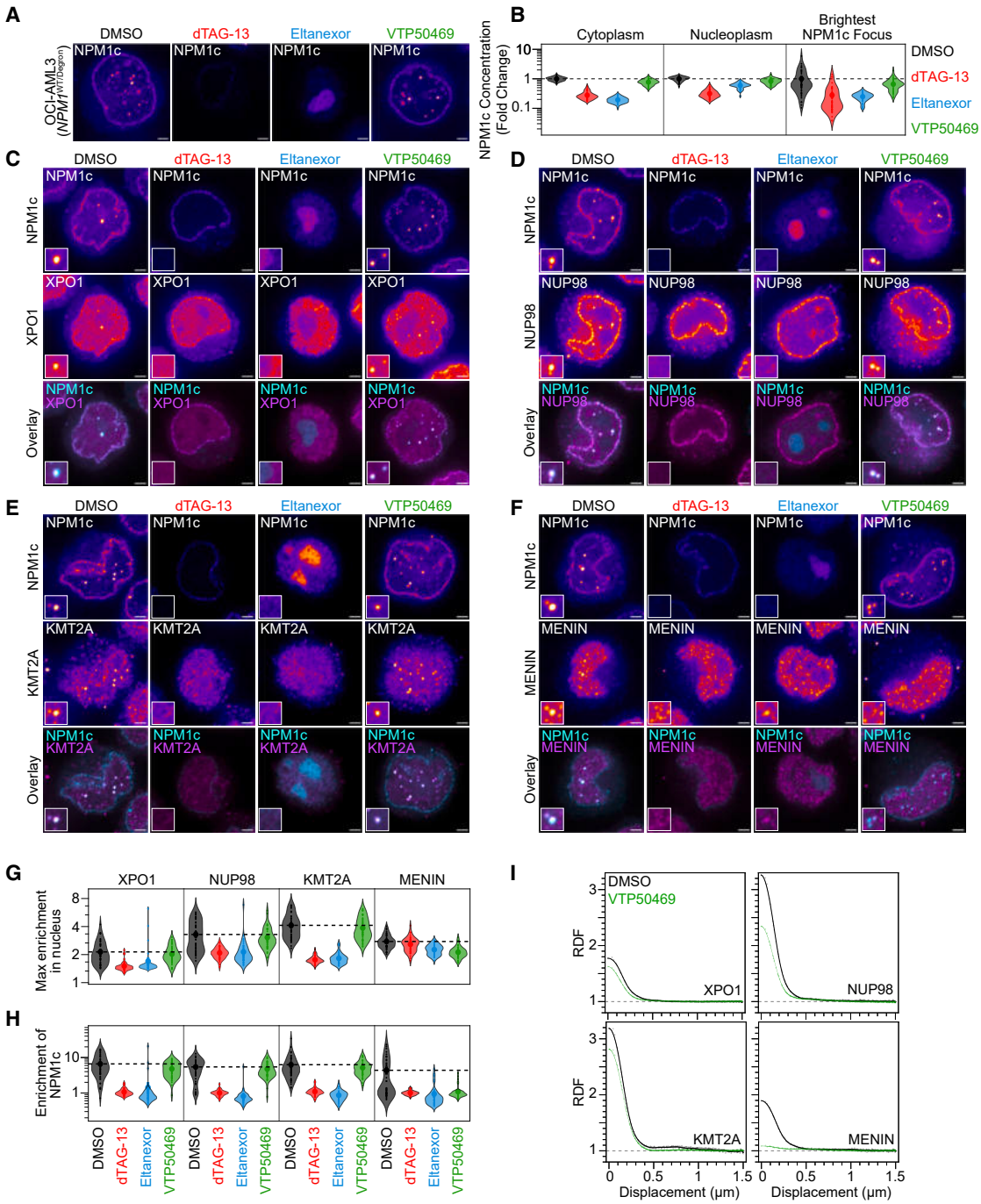

Figure 3. NPM1c condensates are necessary for protein recruitment

(A) Live imaging of *NPM1*$^{WT/Degron}$ OCI-AML3 cells following treatments.

(B) NPM1c concentration at indicated compartments and treatments normalized to DMSO controls (n = 50).

(C–F) Images of NPM1c-muGFP and immunostained proteins after indicated treatments.

(G) Max protein enrichment in the nucleoplasm (n = 50).

(H) NPM1c enrichment at max enriched region of interest (ROI) from (G) (n = 50).

(I) RDF of indicated proteins with DMSO or VTP50469 treatment from the center of NPM1c condensates (n = 50). All cells were treated for 24 h with DMSO or indicated treatments (dTAG-13 = 500 nM, Eltanexor = 100 nM, VTP50469 = 300 nM). All images are shown in Fire LUT except colocalization (cyan and magenta). Scale bars, 2 μm. Insets are magnified 2 μm square regions. RDF shaded regions are mean fit confidence intervals.

See also Figures S3 and S4.

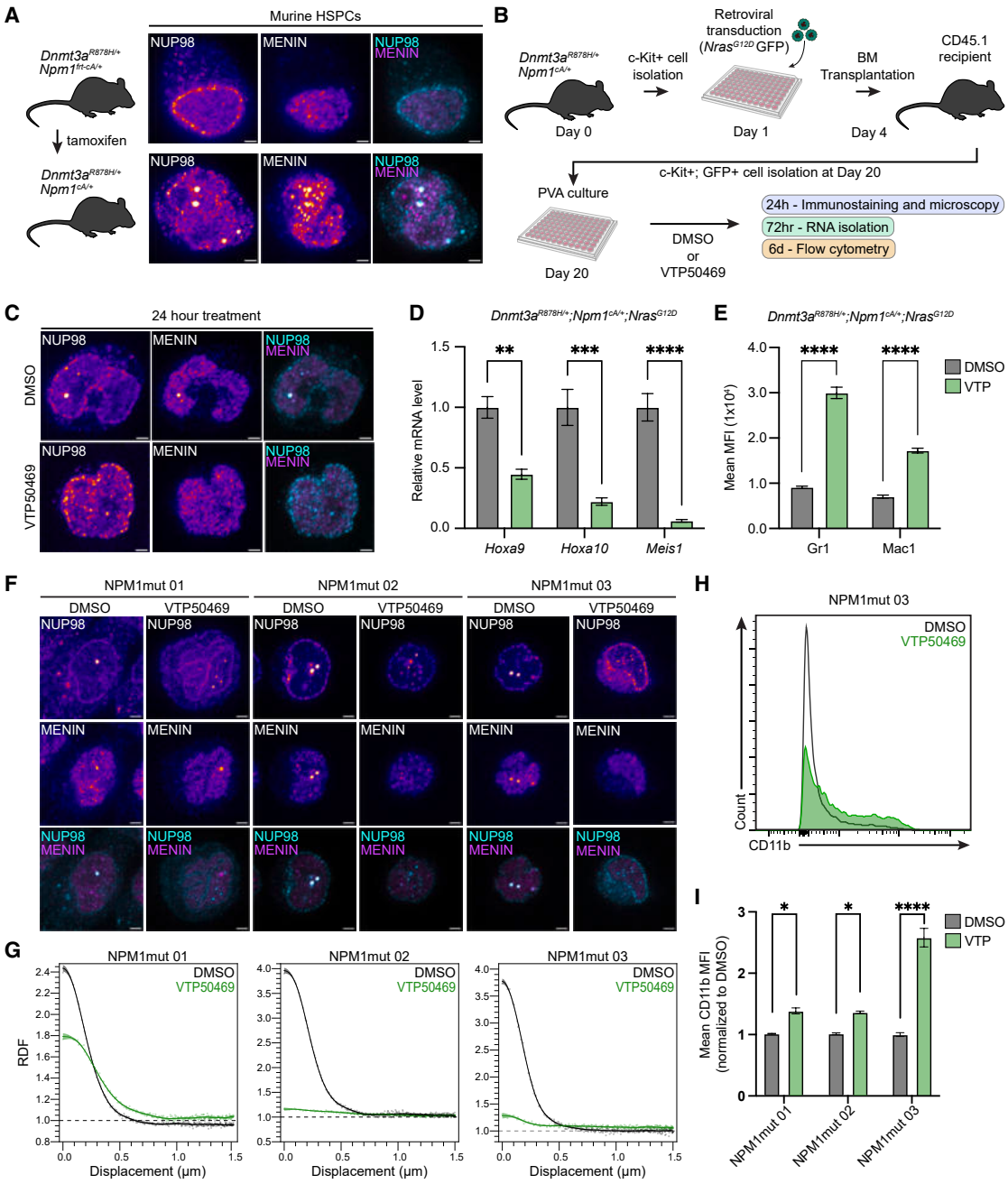

Figure 4. C-body composition dictates leukemic features in primary murine and human cells

(A) Npm1c induction with tamoxifen in mice (left) and immunostaining of HSPCs isolated from Npm1frt-cA and Npm1c donor mice with indicated antibodies.

(B) Schematic representation of *ex vivo* studies.

(C) Immunostaining of murine HSPCs treated with DMSO or VTP50469 *ex vivo* with indicated antibodies.

(D and E) (D) *Ex vivo* results for real-time qPCR analysis of mRNA levels and (E) flow cytometry analysis of myeloid differentiation markers.

(F) Immunostaining of human AML patient cells with VTP50469.

(G) RDF of MENIN around NUP98 center following VTP50469 treatment (n = 20–60 cells per sample).

(H and I) (H) Representative histogram of CD11b level and (I) fold change of mean CD11b intensity in patient samples relative to DMSO. All cells were treated at the same concentrations for 24 h prior to imaging. Flow cytometry analysis was performed at days 3 and 6 in human and murine cells, respectively. All images are shown in Fire LUT except colocalization (cyan and magenta). Scale bars, 2 μm. Insets are magnified 2 μm square regions. RDF shaded regions are mean fit confidence intervals. Error bars, standard error (D) or standard deviation (E and I). *p < 0.05, **p < 0.01, ***p < 0.001, ****p < 0.0001, two-way ANOVA.

Next, we examined peripheral blood from *NPM1*-mutant AML patients (Table S2). Immunostaining of mononuclear cells revealed C-bodies across all samples (Figure 4F). MENIN inhibition led to MENIN loss from C-bodies and a corresponding shift toward monocytic differentiation (Figures 4F–4I), consistent with our observations *in vitro* and *in vivo* (Figures 3 and 4C). Thus, we conclude that C-body composition is strongly associated with leukemogenic gene expression and differentiation in *NPM1*-mutant AML.

Heterotypic phase separation drives C-body formation

Our data show that XPO1 and MENIN inhibitors alter C-body formation and composition, respectively, and that C-bodies play an integral role in leukemogenesis. We therefore investigated the biophysical determinants of NPM1c driving C-body formation.

Phase separation is a concentration-dependent process defined by the presence of a phase boundary at a saturation concentration (C_{sat}) above which condensate formation is favorable.[20] In multi-component phase separation driven by heterotypic interactions, stoichiometric imbalance in one component can alter condensate composition, size, and function, a phenomenon referred to as heterotypic destabilization.[22]

To assess whether C-bodies are phase-separated condensates driven by heterotypic interactions, we examined their concentration-dependent behavior using a lentiviral system to overexpress full-length NPM1c (FL-NPM1c) in *NPM1*$^{WT/Degron}$ OCI-AML3 cells (STAR Methods). While low FL-NPM1c expression had no effect on C-bodies or nuclear periphery enrichment, high FL-NPM1c expression produced larger C-bodies and reduced nuclear periphery enrichment, suggestive of heterotypic destabilization (Figure S5A). Degradation of endogenous NPM1c with dTAG-13 resulted in loss of C-bodies in all cells except those with highly expressed FL-NPM1c, suggesting a threshold expression level (C_{sat}) for C-body formation (Figure S5B). By contrast, overexpression of the fluorescent protein alone did not impact endogenous NPM1c or C-body formation (Figures S5C and S5D).

Heterotypic destabilization results in a non-fixed C_{sat}, causing excess molecules in the dilute phase.[22] For example, nucleoli dissolve during prophase, flooding the nucleoplasm with excess NPM1wt (Figure 1H). Likewise, we hypothesized that C-body destabilization would increase cytoplasmic levels of NPM1c due to XPO1-mediated export of NPM1c released into the nucleoplasm. Consistent with our observations of NPM1c condensate loss in prophase (Figure S1G), FL-NPM1c overexpression increases cytoplasmic export of endogenous NPM1c (Figure S5E). These data indicate that C-bodies are driven by heterotypic phase separation.

Finally, we examined whether C-body destabilization impaired cell growth and differentiation. Cells overexpressing FL-NPM1c had reduced growth over time compared with cells expressing the fluorescent protein alone (Figures S5F and S5G), suggesting decreased cell fitness. Upon dTAG-13 treatment, FL-NPM1c overexpression prevented cellular differentiation, indicating that FL-NPM1c is functionally indistinguishable from endogenous NPM1c (Figures S5G and S5K). Notably, despite enhanced localization of endogenous NPM1c to the cytoplasm, cells exhibited decreased growth (Figure S5F). Together, these data suggest that C-body stability dictates cell growth and the leukemic state.

Heterotypic destabilization of C-bodies decreases cell growth

To better understand NPM1c's role in condensate formation and cancer cell fitness, we focused on NPM1c protein architecture. NPM1 has an oligomerization (self-pentamerization) domain, a conserved IDR with alternating acidic and basic stretches, and a C-terminal domain (CTD) that folds into an RBD.[26,59] Although *NPM1* mutations only alter the last few residues of NPM1wt, they cause unfolding of the CTD.[30] To discern which domains contribute to C-body formation, we used a lentiviral system to express truncated NPM1c proteins in *NPM1*$^{WT/Degron}$ OCI-AML3 cells (Figures 5A and 5B; STAR Methods).

All proteins displayed cytoplasmic localization (Figure 5A). Truncated proteins exhibited a range of C-body partition coefficients (Figure 5C). Consistent with previous findings, NPM1cΔNES was also observed in the nucleolus (Figure 5A).[35] All truncated proteins enhanced cytoplasmic export of endogenous NPM1c; however, FL-NPM1c, ΔA3, ΔB2, and ΔCTD had a substantially greater effect (Figures S5E and S5D). C-body partitioning (K) strongly correlated with cytoplasmic export of endogenous NPM1c ($\rho = 0.88$; Figure 5E). In this way, proteins that favorably drive heterotypic phase separation destabilize C-bodies, resulting in displacement of endogenous NPM1c from condensates and enhanced cytoplasmic export. These data suggest that multiple domains of NPM1c can contribute to heterotypic destabilization of endogenous condensates, in accordance with multivalent interactions needed for phase separation.

Next, we questioned whether cytoplasmic export of endogenous NPM1c influenced cell growth as in Figure S5F. We observed cell growth for approximately 2 weeks and identified two discrete behaviors (Figure 5F). Cells expressing ΔA2, ΔB1, and NPM1cΔNES had a minor decrease in growth compared with the mCherry control, while cells expressing FL-NPM1c, ΔA3, ΔB2, ΔCTD, and NPM1wt+NES had substantially decreased growth. Growth rate was negatively correlated with C-body partitioning and cytoplasmic export of endogenous NPM1c ($\rho = -0.60$ and -0.77; Figures 5G and 5H). Notably, the low partitioning and impaired growth rate observed for ΔCTD and NPM1wt + NES (Figure 5G) suggest they remove interactions needed for phase separation and thus act as caps to destabilize C-bodies through loss of valence as seen in other contexts.[24] Together, these data suggest that heterotypic destabilization of C-bodies impairs cell fitness.

C-bodies are necessary for leukemia cell survival *in vitro* and *in vivo*

These results led us to ask whether any NPM1c truncation forms C-bodies without endogenous NPM1c. To this end, we expressed each truncation in *NPM1*$^{WT/Degron}$ OCI-AML3 cells and treated with dTAG-13 to degrade endogenous NPM1c (Figures 6A and S6B). Only FL-NPM1c, ΔA3, and ΔB2 formed condensates, suggesting that A3 and B2 domains are dispensable for C-body formation. ΔCTD, ΔA2, and ΔB1 were unable to maintain C-bodies, suggesting that these regions are required. NPM1wt + NES did not form C-bodies, indicating that XPO1 binding to a C-terminal NES on NPM1wt is insufficient for aberrant phase separation. Finally, we did not observe C-body formation by

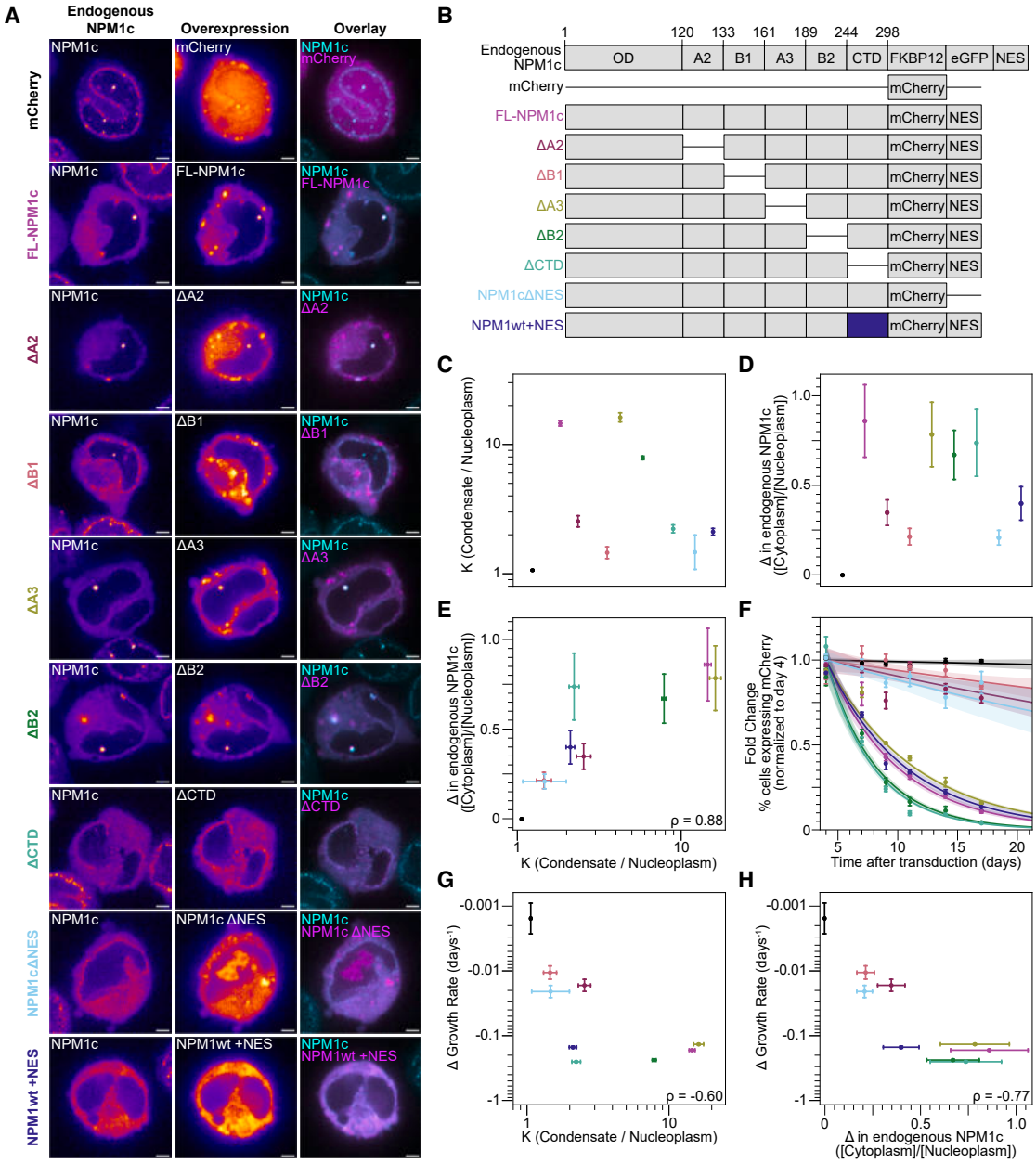

Figure 5. C-body destabilization enhances NPM1c export and reduces growth

(A) Live *NPM1*$^{WT/Degron}$ OCI-AML3 cells (DMSO treatment) expressing NPM1c truncations.

(B) Schematic of NPM1c truncation series.

(C) Partitioning (K) of each truncation.

(D) Instantaneous change (as in Figure S5E) in endogenous NPM1c cytoplasm/nucleoplasm ratio.

(E) Correlation between partitioning and change in endogenous NPM1c ratio.

(F) Fold change of % cells expressing truncations over 17 days (normalized to day 4), measured by flow cytometry, $n = 3$ biological replicates per truncation.

(G and H) (G) Correlation of change in growth rate (shown as days^{-1}) with partitioning into C-bodies and (H) change in endogenous NPM1c ratio. $n > 40$ for (C)–(E), (G), and (H). ρ is the Spearman correlation coefficient. Error bars indicate fit parameter standard error. Images are shown in Fire LUT except colocalization (cyan and magenta). Scale bar, 2 μm.

See also Figure S5.

NPM1cΔNES. This protein maintains the full amino acid sequence of NPM1c and ostensibly all binding interactions, suggesting that it is a "C-body null" variant of NPM1c.

Notably, FL-NPM1c, ΔA3, and ΔB2 form condensates at higher concentrations indicative of a C_{sat}; however, C-body formation was not observed at any expression level for the

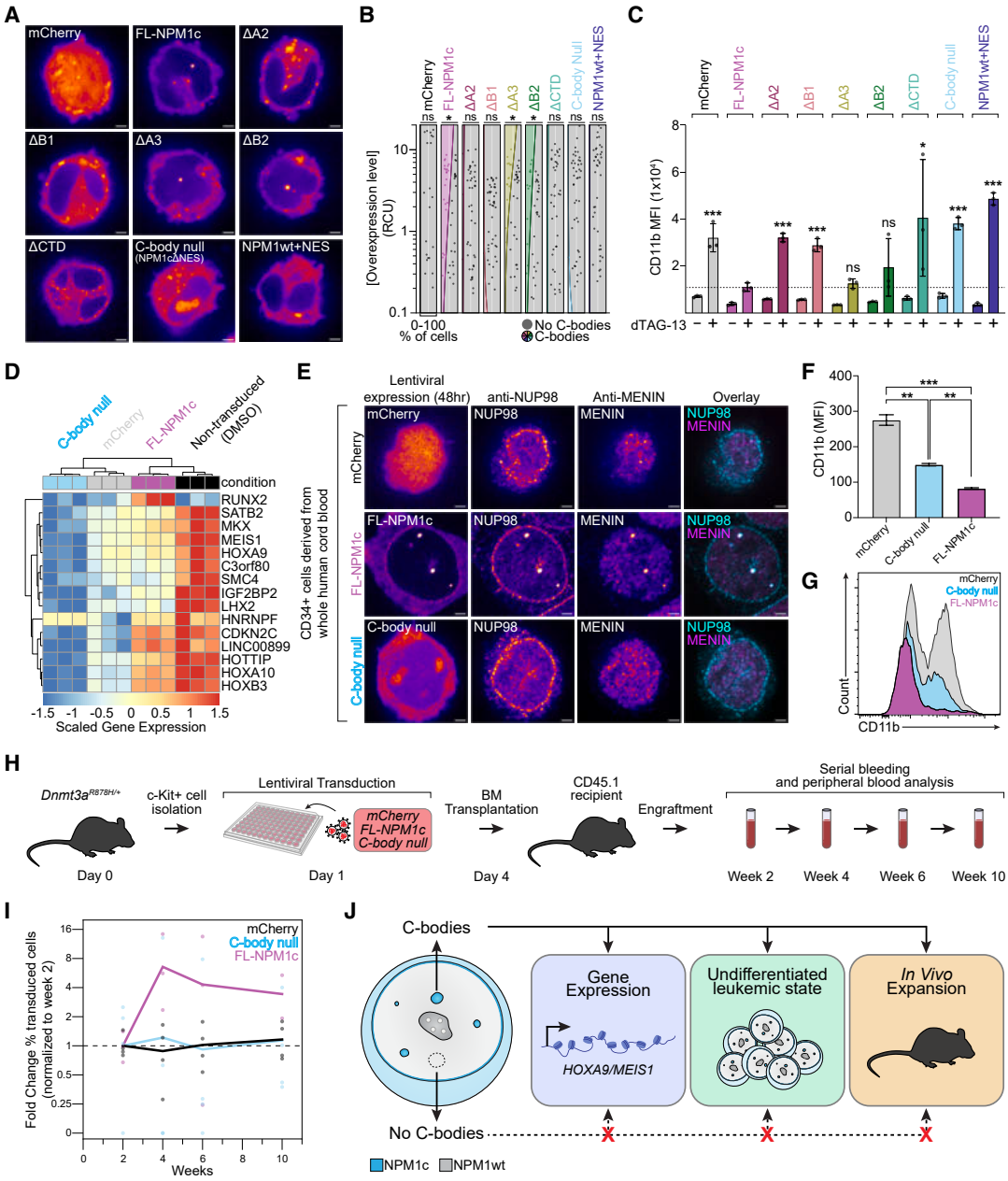

Figure 6. Multiple domains of NPM1c are required for C-body formation and maintaining the disease state

(A) Live *NPM1*$^{WT/Degron}$ OCI-AML3 cells expressing NPM1c truncations after 7 days of dTAG-13 (500 nM) treatment.

(B) NPM1c truncation concentration and condensate formation after dTAG-13 treatment. Shaded regions represent fractions of cells without (gray) or with (multicolor) condensates. Spearman's rank test, $^{*}p < 0.05$, $n > 40$.

(C) CD11b median fluorescence intensity (MFI) via flow cytometry after 14-day treatment, $n = 3$ biological replicates per treatment and truncation. The dashed line indicates the mean MFI for FL-NPM1c.

(D) Heatmap and hierarchical clustering of C-body target gene expression (see Figure S3B).

(E) Immunostaining of CD34^{+} cord blood cells expressing indicated truncations.

(F and G) (F) CD11b MFI and (G) representative CD11b intensity histograms of CD34^{+} cord blood cells expressing indicated truncations.

(H) Schematic depicting NPM1c overexpression in murine HSPCs harboring mutant *Dnmt3a*.

(I) Fold change of donor cells expressing NPM1c in the peripheral blood of mice (n = 3–4 per group).

(J) Schematic depicting the role of C-bodies in human and murine primary cells. All images are shown in Fire LUT except colocalization (cyan and magenta). Scale bars, 2 μm. Error bars, mean ± standard deviation. $^{*}p < 0.05$, $^{**}p < 0.01$, $^{***}p < 0.001$, Z test.

See also Figures S5 and S6.

remaining truncations (Figure 6B). All proteins maintained strong enrichment in the cytoplasm (Figures 6A and S5H). These results indicate that C-body formation depends on several domains of NPM1c, consistent with multivalent interactions needed for heterotypic phase separation.

We next asked which variants could prevent cells from differentiating following endogenous NPM1c degradation by measuring a monocytic differentiation marker (CD11b). After 2 weeks, only cells expressing truncations that form C-bodies showed minimal CD11b expression, maintaining an undifferentiated leukemic state (Figure 6C). Importantly, cells expressing the C-body null variant also differentiated (Figure 6C). All truncations showed cytoplasmic localization, yet only those forming C-bodies maintained minimal CD11b expression, indicating that C-bodies are required to prevent differentiation.

To validate the connection between C-bodies, monocytic differentiation, and the leukemic transcriptional program, we analyzed RNA sequencing (RNA-seq) data obtained from *NPM1*$^{WT/Degron}$ OCI-AML3 cells expressing FL-NPM1c, C-body null, or mCherry constructs after endogenous NPM1c degradation. We clustered samples according to expression of overlapping NPM1c target genes (Figures S3B and S6C), revealing that only FL-NPM1c maintains expected gene expression (Figure 6D). These data establish that C-bodies are essential for the leukemic transcriptional program.

Next, we examined whether *de novo* C-bodies in normal human blood cells could establish the NPM1c-specific leukemic phenotype. We introduced FL-NPM1c, C-body null, or mCherry into CD34^{+} cells isolated from human umbilical cord blood. As expected, only FL-NPM1c formed *de novo* C-bodies, and all proteins showed cytoplasmic localization (Figure 6E). When allowed to differentiate toward monocytic lineages with conditioned media (STAR Methods), only FL-NPM1c prevented differentiation (Figures 6F, 6G, and S6D). These data underscore the necessity of C-bodies for maintaining a stem-cell-like state.

To determine if C-bodies are essential for engraftment and *in vivo* expansion of *NPM1*-mutant AML, we expressed FL-NPM1c, C-body null, or mCherry in *Dnmt3a*-mutant murine HSPCs and transplanted them into wt recipient mice (Figure 6H; STAR Methods). While all transplants engrafted, only cells expressing FL-NPM1c expanded in the peripheral blood and persisted over 10 weeks (Figures 6I and S6E).

Thus, we conclude that NPM1c phase separation is necessary for the maintenance of the stem-like phenotype observed in leukemia cells, leukemic gene expression, and cellular expansion *in vitro*, *ex vivo*, and *in vivo* in both human and murine models (Figure 6J).

Multiple leukemogenic fusion proteins drive C-body formation

Our data demonstrate that C-bodies enrich proteins that facilitate leukemogenesis. Notably, chromosomal rearrangements of *NUPs* and *KMT2A* can generate oncofusion proteins driving subtypes of leukemias with characteristic *HOXA*/*MEIS1* gene expression.[60–62] NUP98-fusion proteins can even form condensates, and some have reported on the potential of KMT2A oncofusions to phase separate.[15,18] NUP and KMT2A fusion proteins are thought to work alongside MENIN and XPO1 to regulate gene expression.[55,63] Given the overlap of protein complexes associated with leukemias driven by NPM1c and oncofusions, we asked if oncofusion-driven condensates recruited XPO1, NUP98, KMT2A, and MENIN, and whether these condensates were structurally similar to NPM1c-driven C-bodies.

We first expressed NUP98::NSD1 and SET::NUP214 oncofusions in U2OS cells, observing *de novo* nuclear puncta (Figure 7A) consistent with reports.[15,63] Similarly, KMT2A::AFF1 oncofusion expression in U2OS cells resulted in previously unreported puncta (Figure 7A). Immunostaining revealed that NUP98::NSD1 and SET::NUP214 condensates were sufficient to recruit XPO1, NUP98, KMT2A, and MENIN (Figures 7B, 7C, S7A, and S7B), consistent with NPM1c-driven C-bodies (Figures S2D and S2E). KMT2A::AFF1 condensates were sufficient to recruit XPO1, NUP98, and MENIN; however, KMT2A enrichment was not observed. Moreover, we examined LOUCY cells—a T cell acute lymphoblastic leukemia (T-ALL) line—which harbor nuclear SET::NUP214 condensates. We observed focal enrichment of XPO1, KMT2A, and MENIN consistent with previous reports[63] and identified NUP98 recruitment to these condensates (Figures S7C and S7D). HL-60 cells, which lack NUP or *KMT2A* oncofusion-encoding mutations, did not display highly enriched nuclear puncta (Figures S7C and S7D).

Finally, we asked whether these oncofusion condensates are indeed C-bodies. Our observation that NPM1c and oncofusion condensates recruit a common set of proteins strongly supports their convergence on C-bodies. However, separate coexisting condensates can share protein partners, such as DDX6 in P-bodies and stress granules, or Fibrillarin in Cajal bodies and nucleoli.[24,64,65] To determine if multiple condensates are scaffolded from similar interactions in cells, we formalized our observations into a new quantitative miscibility assay, grounded in polymer physics, that experimentally probes the phase diagram for independent drivers of phase separation (Figures S7E–S7I).

For example, if interaction networks driving oncofusion and NPM1c condensates are separable, then two distinct phases (i.e., two types of coexisting condensates) will be achievable within a cell. By contrast, if interaction networks are highly interdependent, then only one phase will ever be achieved (i.e., one type of mixed condensate) within a cell, despite some compositional differences between different cells. To avoid loss of generality under this framework, we define these two cases as biophysically distinguishable or indistinguishable, respectively (Figure 7D).

Employing this new assay, we coexpressed oncofusions with NPM1c in U2OS cells (Figure 7E). At all expression levels where phase separation occurs, we observed a single type of mixed condensate containing NPM1c and oncofusion proteins within each cell, indicating that these condensates are biophysically indistinguishable nuclear structures (Figures 7F–7H). Together with the recruitment of a shared network of interaction partners, these findings imply that NUP/KMT2A oncofusion condensates are indeed C-bodies. As demonstrated here in *NPM1*-mutant AML, we propose that C-bodies driven by oncofusions may play a role in driving disease across multiple subtypes of leukemia.

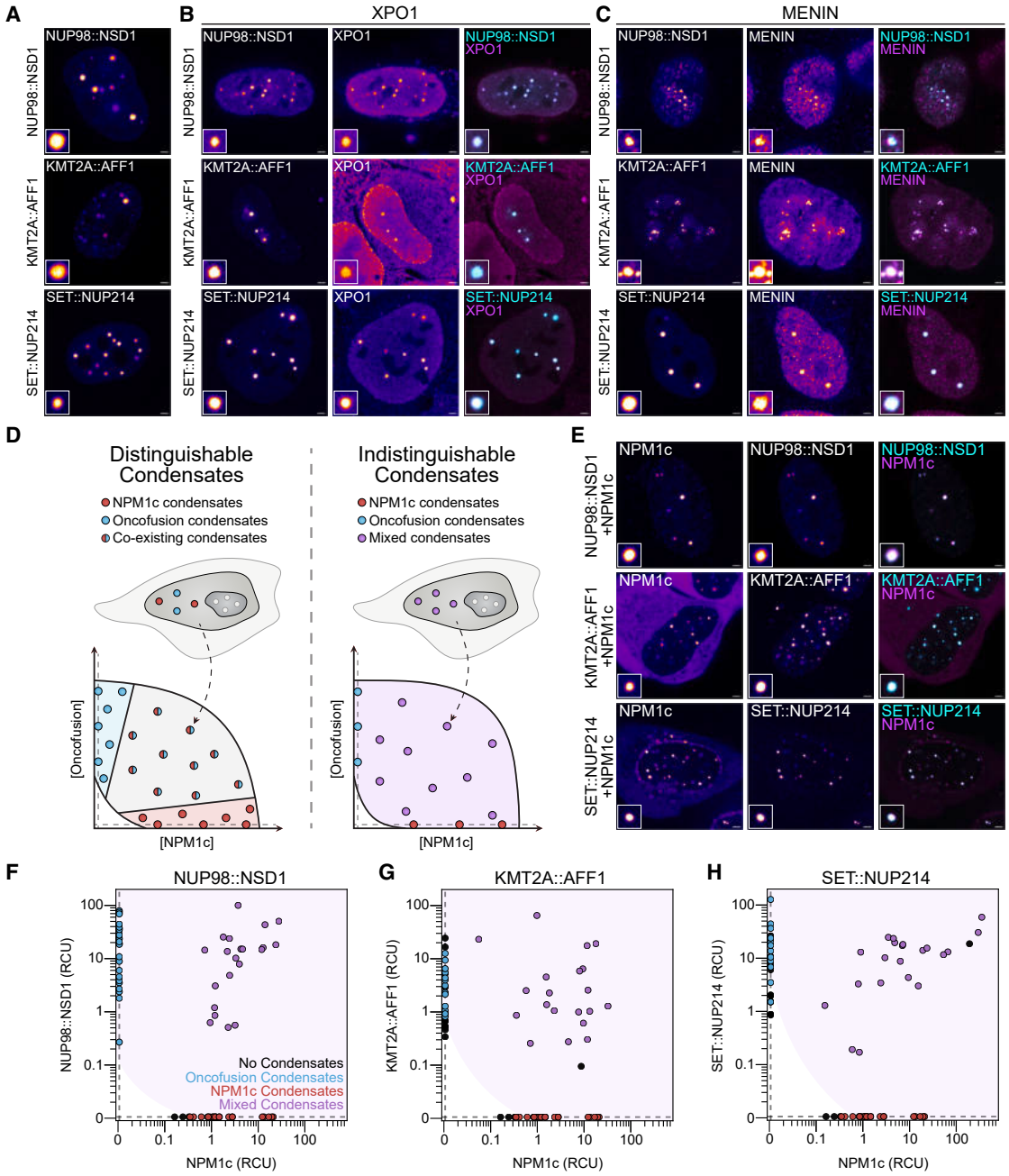

Figure 7. Independent drivers of phase separation converge on C-body formation in leukemia

(A) Live U2OS cells expressing oncofusion proteins.

(B and C) (B) Immunostaining of U2OS cells expressing oncofusion proteins targeting XPO1 and (C) MENIN.

(D) Schematic representation of biophysical assay to identify condensate miscibility in cells. Plots depict phase diagrams (based on Figure S7) in which co-expression of individual proteins yields coexisting (distinguishable) or mixed (indistinguishable) condensates. Shaded regions indicate distinct phases. Dots indicate NPM1c condensates (red), oncofusion condensates (blue), coexisting condensates (red and blue), or mixed condensates (purple). Points on axes represent cells expressing only one protein and have been shifted (dashed line).

(E) Live U2OS cells expressing NPM1c and individual oncofusion proteins.

(F–H) Experimental phase diagrams quantifying concentration in the nucleoplasm in individual cells expressing oncofusions, NPM1c, or both. Black dots indicate cells without nuclear condensates, and the remaining colors are as indicated in (D). Shaded regions highlight approximate phase boundaries. Points on axes represent cells expressing only one protein and have been shifted (dashed line). NPM1c-only data from *x* axes is repeated in all 3 panels. All images are shown in Fire LUT except colocalization (cyan and magenta). Scale bars, 2 μm. Insets are magnified 2 μm square regions.

See also Figure S7.

DISCUSSION

NPM1 mutations drive approximately one-third of newly diagnosed cases of adult AML,[27,28] but how does cytoplasmic NPM1c paradoxically influence gene expression in the nucleus? What is the relationship between NPM1c localization and its role in leukemic transformation? Do other leukemia subtypes with similar gene expression profiles share a mechanistic basis? In this study, we show that NPM1c forms phase-separated nuclear condensates—termed coordinating bodies or C-bodies—across multiple models of *NPM1*-mutant AML. We find that C-bodies are necessary for driving *NPM1*-mutant AML. Finally, we report that leukemogenic oncofusion proteins found in other subtypes of leukemias form nuclear structures that are biophysically indistinguishable from NPM1c-driven C-bodies, suggesting that C-bodies are a unifying feature of multiple subtypes of leukemia.

C-bodies drive *NPM1*-mutant AML

Despite its pathognomonic cytoplasmic localization, NPM1c's essential place of action for driving leukemia has remained murky. Indeed, studies over the last two decades have focused on aberrant localization of NPM1c that may lead to loss of function of nuclear and nucleolar proteins or gain of function in the cytoplasm and nucleoplasm.[36–38,55,66–69] Here, we show for the first time that NPM1c forms C-bodies, a new condensate observed across *in vitro* and *in vivo* models of *NPM1*-mutant AML, and multiple primary *NPM1*-mutant AML patient samples. While NPM1c enrichment within distinct cellular compartments showed some variation across all tested models, the greatest concentration of NPM1c was invariably found in C-bodies. Our data demonstrate C-bodies are necessary for all hallmarks of this disease: maintaining leukemic gene expression, preventing differentiation, and promoting expansion *in vivo*. Critically, NPM1c localization in the cytoplasm, nucleoplasm, or nucleolus is not sufficient to promote the leukemic phenotype, establishing C-bodies as the primary driver of leukemogenesis.

How do C-bodies work? Reports have shown that NPM1c degradation causes rapid reduction of transcription from NPM1c-bound target genes and alters chromatin modifications,[35–37] yet a specific mechanism of action has not been resolved. In our previous work, we speculated that NPM1c may act on chromatin.[35] Here, we identified several proteins—including XPO1, NUP98, KMT2A, and MENIN—that localize to NPM1c-driven C-bodies and *HOXA/MEIS1* chromatin. While these proteins may bind to hundreds of chromatin regions independently, we speculate that phase-separated C-bodies selectively regulate a small but consequential list of leukemia-driving genes, similar to other aberrant transcriptional condensates.[70] Indeed, C-bodies enrich at active chromatin regions like the *HOXA9* locus. Critically, *de novo* NPM1c-driven C-bodies recruit associated proteins in multiple genetic contexts *in vitro* and *in vivo*. C-body destabilization or changes in composition reduce chromatin binding, lower *HOXA/MEIS1* gene expression, and promote monocytic differentiation. Although we cannot exclude a cytoplasmic role for NPM1c,[39] our extensive truncation series reveals that C-body formation is essential for maintaining the leukemic phenotype, and cytoplasmic NPM1c is not sufficient. Indeed, employing the C-body null variant of NPM1c, we show that C-bodies are essential for cellular expansion *in vitro* and *in vivo*. Together, our data suggest C-bodies drive *NPM1*-mutant AML through the sequestration of NUP98 and other proteins such as the COMPASS-like methyltransferase complex—which includes KMT2A and MENIN—maintaining activation of developmentally regulated genes in leukemia.[60,71]

Our study provides insight into the mechanism of action of targeted therapies with clinical promise in *NPM1*-mutant AML. XPO1 inhibitors break the NPM1c-XPO1 interaction, leading to relocalization of NPM1c from the cytoplasm to the nucleolus.[29,31,72] Here, we further demonstrate XPO1 inhibition dissolves C-bodies. Our truncation series decouples NPM1c-XPO1 interaction and cytoplasmic export, suggesting that the efficacy of XPO1 inhibitors is a result of C-body disruption rather than export inhibition. Similarly, MENIN inhibitors are a leading class of therapies that break KMT2A-MENIN interactions and disrupt aberrant chromatin activation, yet their precise mechanism in *NPM1*-mutant AML is unclear.[40–42,56] We show that MENIN inhibitors cause MENIN—but not KMT2A—depletion from C-bodies, despite persistence of MENIN puncta elsewhere in the nucleus. To this end, we propose that the critical interaction between MENIN and KMT2A occurs within C-bodies. Indeed, MENIN inhibitor treatment reduces chromatin binding and expression of C-body-bound genes and shifts cells toward differentiation *in vitro, in vivo*, and in primary *NPM1*-mutant AML patient samples. Broadly, our results indicate that targeting of C-body formation or function may be a promising therapeutic strategy in *NPM1*-mutant AML.

Our findings have additional implications for aspects of *NPM1*-mutant disease. Notably, heterozygous loss of *NPM1* (e.g., del (5q)) is associated with myelodysplastic syndromes and genome instability, yet *NPM1*-mutant AMLs typically have a normal karyotype.[73] Our observation that NPM1c colocalizes with NPM1wt at the chromosomal sheath during mitosis may indicate that its function in maintaining genome stability is preserved. Separately, our observation that NPM1c overexpression drives *de novo* C-body formation suggests that common co-mutations (e.g., in *DNMT3A* or *TET2*)[74,75] are not required for C-body formation but instead functionalize C-bodies through altered gene expression or chromatin accessibility.

Heterotypic interactions dominate NPM1 phase separation

Phase separation driven by weak multivalent interactions is a general paradigm underlying many membrane-less compartments within cells.[23,46] In this context, our observation of the strong spatial separation between NPM1c and NPM1wt—which are >95% identical—is largely unexpected, as these proteins ostensibly share weak interactions. Strikingly, their separation is imposed by the cell cycle, where during telophase, NPM1c and NPM1wt relocate from the chromosomal sheath to C-bodies and PNBs, respectively. Throughout interphase, this separation is enforced by the immiscibility (i.e., exclusivity) of distinct interaction networks (e.g., rRNA in ribosomal intermediates or the NUP98/COMPASS complex) coordinated by NPM1wt and NPM1c.

How does a small change in amino acids at the C terminus encode this separation? NPM1 has a self-pentamerization domain, which enables multivalent interactions through its charge-blocky IDR and RBD domains. The IDR, unchanged in NPM1c, facilitates recruitment to the chromosomal sheath during mitosis,[76] consistent with our observations. By contrast, the RBD is essential for NPM1wt's role in nucleolar formation and is mutated into an XPO1-binding NES in NPM1c.[22,26,27] While our data suggests that interaction with XPO1 is sufficient to decimate enrichment into nucleoli, this interaction is insufficient to form *de novo* C-bodies. Indeed, our truncation series illuminates multiple regions of NPM1c necessary for C-body formation. This suggests that additional interaction partners, with less affinity for NPM1wt, contribute to C-body formation.

Endogenous condensates rely on interaction networks (i.e., heterotypic interactions) and thus exhibit composition-dependent stability.[22,24] Similarly, we find that overexpression (i.e., compositional overrepresentation) of NPM1c and relevant truncations destabilizes C-bodies and results in decreased cell growth. Together, these data demonstrate that C-bodies are also driven by heterotypic interactions.

C-bodies as a common therapeutic target across leukemia subtypes

Phase separation is an emerging feature of many leukemias, where dozens of genetic alterations involving NUP genes, *KMT2A*, *ENL*, and others are reported to cause condensate formation.[14,15,18,60,61,77,78] Broadly, hundreds of mutant proteins are proposed to drive phase separation in disease, but whether there is functional redundancy between condensates remains an open question.[17] Consolidating unrelated mutant proteins as independent drivers of the same functional condensate would clarify disease mechanisms. Toward this end, we develop a simple assay—grounded in polymer physics—to determine whether independent proteins form the same indistinguishable condensate. Remarkably, this approach revealed that many leukemic oncofusions also drive C-body formation, suggesting that C-bodies are a common feature of many leukemias. Further studies using *in vivo* models are needed to characterize the role of C-bodies in oncofusion-driven leukemias. Phase separation underlies aberrant chromatin regulation in a growing list of leukemias driven by fusion oncoproteins.[79] We anticipate that this conceptual framework will be applicable in many contexts and enable the identification of pathogenic condensates underlying various diseases.

How do the principles of multi-component phase separation inform strategies for targeting oncogenic condensates? We show that C-bodies rely on a network of interactions to form and function. We anticipate that new or existing drugs disrupting proteins in this network will destabilize condensates and therefore demonstrate clinical activity. As an example, XPO1 and MENIN inhibitors have already shown activity across *NPM1*-mutant, *NUP98*-fusion, and *KMT2A*-rearranged leukemias, likely owing to their shared impact on C-bodies.[40–42,52,72,80] Notably, some patients develop mutations at the MENIN-KMT2A interface that confer resistance to MENIN inhibitors, highlighting the value of new approaches targeting C-bodies.[81] Future investigation into the composition and dynamics of C-bodies and other pathogenic condensates will be crucial for the development of effective therapies.

Limitations of the study

While we show that C-bodies drive leukemic features of *NPM1*-mutant AML in all tested models, additional experiments are needed to establish the existence and role of C-bodies in oncofusion-driven disease using *in vitro* and *in vivo* models as well as primary human samples. We demonstrate here that C-bodies are critical for driving leukemic gene transcription; however, we cannot rule out the possibility that some steps of chromatin regulation can occur outside C-bodies. Nevertheless, NPM1c condensation is essential to maintain the leukemic phenotype. Finally, our study did not fully characterize the complex proteome of C-bodies driven by NPM1c or oncofusion proteins. Additional experiments cataloging all proteins within C-bodies are needed to characterize all network interactions and identify additional therapeutic vulnerabilities in C-body-driven disease.

RESOURCE AVAILABILITY

Lead contact

Further information and requests for resources and reagents should be directed to the lead contact, Joshua A. Riback (josh.riback@bcm.edu).

Materials availability

All materials used in this study are commercially available or available upon request. Human cell lines and mouse models generated by the Riback and/or Goodell laboratories are available upon request and will require a standard materials transfer agreement (MTA).

Data and code availability

All data generated by sequencing methods have been deposited to the Gene Expression Omnibus (GEO) according to accession numbers listed in the key resources table.

ACKNOWLEDGMENTS

We thank Jason Lee for providing microscopy access for pilot studies, the Leukemia Sample Bank at the University of Texas MD Anderson Cancer Center for access to primary patient samples, and Liling Wan and Kyle Eagen for help with DNA FISH experiments. We also thank all members of the Riback and Goodell laboratories and Arzeena S. Ali for useful comments and feedback. This project was supported by CA183252 (M.A.G.), CA26574 (M.A.G.), and F30CA268725 (G.K.D.). J.A.R. is a CPRIT Scholar in Cancer Research with funding from the Cancer Prevention and Research Institute of Texas (CPRIT) New Investigator Grant RR210040 and was supported by the Ted Nash Long Life Foundation, the Leukemia Research Foundation, and the Searle Scholars Program. R.E.R. was supported by K08CA201611 and K12CA090433-11. B.F. was supported by Associazione Italiana per la Ricerca sul Cancro (AIRC). L.B. was supported by Associazione Italiana per la Ricerca sul Cancro (AIRC) start-up grant no. 22895. V.A. was supported by the Trond Mohn Foundation and The Research Council of Norway (project no. 303358). B.T.G. was supported by the Norwegian Cancer Society (grant no. 303445 and 19017), the Research Council of Norway (project no. 303358), and Helse Vest Health Trust (project no. F-13102). This work was also supported by the Cytometry and Cell Sorting Core with funding from CPRIT and the NIH (RP180672, CA125123, and RR024574). N.S. was supported by the Andrew Sabin Family Foundation Fellowship. S.S.Y. was supported by a Scialog Award sponsored jointly by the Research Corporation for Science Advancement and the Gordon and Betty Moore Foundation (award no. 28418). N.S. is a CPRIT Scholar in Cancer Research with funding from the Cancer Prevention and Research Institute of Texas (CPRIT) New Investigator Grant RR160021 and RP220292.

AUTHOR CONTRIBUTIONS

Conceptualization, G.K.D., M.A.G., and J.A.R.; methodology, G.K.D., A.A., E.K., C.-W.C., E.P., M.A.G., and J.A.R.; investigation, G.K.D., A.A., E.K., J.B., M.S., N.C., G.L., C.D., A. Martell, A.G., K.W., and N.S.; formal analysis, G.K.D., E.L., C.-W.C., J.D.L.F., and J.A.R.; data curation, G.K.D., C.-W.C., S.S.Y., J.D.L.F., and J.A.R.; resources, A. Maiti, S.S.Y., N.J.S., N.S., V.A., B.T.G., and B.F.; writing – original draft, G.K.D., M.A.G., and J.A.R.; writing – review and editing, G.K.D., A.A., E.K., J.B., M.S., C.-W.C., E.P., R.E.R., L.B., N.S., M.A.G., and J.A.R.; supervision, R.E.R., L.B., M.A.G., and J.A.R.

DECLARATION OF INTERESTS

The authors declare no competing interests.

STAR★METHODS

Detailed methods are provided in the online version of this paper and include the following:

- KEY RESOURCES TABLE
- EXPERIMENTAL MODEL AND STUDY PARTICIPANT DETAILS
  - Cell Culture
  - Propagation of Patient Derived Xenograft Model (PDX2)
  - Primary acute myeloid leukemia samples
  - Mice
  - CRISPR/Cas9 Genetic Engineering
- METHOD DETAILS
  - High-Resolution Microscopy
  - Live Cell Microscopy
  - Immunostaining of human cell lines, PDX models, and primary patient samples
  - Cut-and-run Sequencing
  - Pharmacological disruption of condensate formation and composition
  - Lentiviral Plasmid Generation for Truncation Screen
  - Lentivirus Generation for Truncation Screen
  - NPM1c Truncation Screen
  - Retrovirus Generation for murine HSPCs transduction
  - Transfection of U2OS cells
  - DNA FISH
  - *Ex vivo* VTP50469 treatment of murine HSPCs
  - Flow cytometry analysis
  - qPCR analysis
  - Lentiviral and retroviral transduction of murine HSPCs
  - Immunoblotting
  - RNA isolation and sequencing
  - Selection and determination of fusion protein sequences
- QUANTIFICATION AND STATISTICAL ANALYSIS
  - Quantitative Microscopy
  - Concentration of NPM1wt and NPM1c within the cell
  - ROI determination in live or fixed cells
  - Quantification of brightest puncta enrichment and radial distribution function in live or fixed cells
  - Fitting microscopy data
  - Cut-and-run Sequencing Analysis
  - RNA Sequencing

SUPPLEMENTAL INFORMATION

Supplemental information can be found online at https://doi.org/10.1016/j.cell.2025.10.010.

Received: July 13, 2024
Revised: June 12, 2025
Accepted: October 8, 2025
Published: November 4, 2025

REFERENCES

1. Lyon, A.S., Peeples, W.B., and Rosen, M.K. (2021). A framework for understanding the functions of biomolecular condensates across scales. Nat. Rev. Mol. Cell Biol. *22*, 215–235. https://doi.org/10.1038/s41580-020-00303-z.
2. Grisendi, S., Mecucci, C., Falini, B., and Pandolfi, P.P. (2006). Nucleophosmin and cancer. Nat. Rev. Cancer *6*, 493–505. https://doi.org/10.1038/nrc1885.
3. Mitrea, D.M., Cika, J.A., Guy, C.S., Ban, D., Banerjee, P.R., Stanley, C.B., Nourse, A., Deniz, A.A., and Kriwacki, R.W. (2016). Nucleophosmin integrates within the nucleolus via multi-modal interactions with proteins displaying R-rich linear motifs and rRNA. eLife *5*, e13571. https://doi.org/10.7554/eLife.13571.
4. Lindström, M.S. (2011). NPM1/B23: A Multifunctional Chaperone in Ribosome Biogenesis and Chromatin Remodeling. Biochem. Res. Int. *2011*, 195209. https://doi.org/10.1155/2011/195209.
5. Yao, Z., Duan, S., Hou, D., Wang, W., Wang, G., Liu, Y., Wen, L., and Wu, M. (2010). B23 acts as a nucleolar stress sensor and promotes cell survival through its dynamic interaction with hnRNPU and hnRNPA1. Oncogene *29*, 1821–1834. https://doi.org/10.1038/onc.2009.473.
6. Yang, K., Wang, M., Zhao, Y., Sun, X., Yang, Y., Li, X., Zhou, A., Chu, H., Zhou, H., Xu, J., et al. (2016). A redox mechanism underlying nucleolar stress sensing by nucleophosmin. Nat. Commun. *7*, 13599. https://doi.org/10.1038/ncomms13599.
7. Wang, X., and Li, S. (2014). Protein mislocalization: mechanisms, functions and clinical applications in cancer. Biochim. Biophys. Acta *1846*, 13–25. https://doi.org/10.1016/j.bbcan.2014.03.006.
8. Koken, M.H., Puvion-Dutilleul, F., Guillemin, M.C., Viron, A., Linares-Cruz, G., Stuurman, N., de Jong, L., Szostecki, C., Calvo, F., and Chomienne, C. (1994). The t(15;17) translocation alters a nuclear body in a retinoic acid-reversible fashion. EMBO J. *13*, 1073–1083. https://doi.org/10.1002/j.1460-2075.1994.tb06356.x.
9. de Thé, H., Le Bras, M., and Lallemand-Breitenbach, V. (2012). The cell biology of disease: Acute promyelocytic leukemia, arsenic, and PML bodies. J. Cell Biol. *198*, 11–21. https://doi.org/10.1083/jcb.201112044.
10. Banani, S.F., Lee, H.O., Hyman, A.A., and Rosen, M.K. (2017). Biomolecular condensates: organizers of cellular biochemistry. Nat. Rev. Mol. Cell Biol. *18*, 285–298. https://doi.org/10.1038/nrm.2017.7.
11. Hnisz, D., Shrinivas, K., Young, R.A., Chakraborty, A.K., and Sharp, P.A. (2017). A Phase Separation Model for Transcriptional Control. Cell *169*, 13–23. https://doi.org/10.1016/j.cell.2017.02.007.
12. Rosencrance, C.D., Ammouri, H.N., Yu, Q., Ge, T., Rendleman, E.J., Marshall, S.A., and Eagen, K.P. (2020). Chromatin Hyperacetylation Impacts Chromosome Folding by Forming a Nuclear Subcompartment. Mol. Cell *78*, 112–126.e12. https://doi.org/10.1016/j.molcel.2020.03.018.
13. Kosno, M., Currie, S.L., Kumar, A., Xing, C., and Rosen, M.K. (2023). Molecular features driving condensate formation and gene expression by the BRD4-NUT fusion oncoprotein are overlapping but distinct. Sci. Rep. *13*, 11907. https://doi.org/10.1038/s41598-023-39102-9.
14. Song, L., Yao, X., Li, H., Peng, B., Boka, A.P., Liu, Y., Chen, G., Liu, Z., Mathias, K.M., Xia, L., et al. (2022). Hotspot mutations in the structured ENL YEATS domain link aberrant transcriptional condensates and cancer. Mol. Cell *82*, 4080–4098.e12. https://doi.org/10.1016/j.molcel.2022.09.034.
15. Chandra, B., Michmerhuizen, N.L., Shirnekhi, H.K., Tripathi, S., Pioso, B.J., Baggett, D.W., Mitrea, D.M., Iacobucci, I., White, M.R., Chen, J., et al. (2022). Phase Separation Mediates NUP98 Fusion Oncoprotein Leukemic Transformation. Cancer Discov. *12*, 1152–1169. https://doi.org/10.1158/2159-8290.CD-21-0674.
16. Terlecki-Zaniewicz, S., Humer, T., Eder, T., Schmoellerl, J., Heyes, E., Manhart, G., Kuchynka, N., Parapatics, K., Liberante, F.G., Müller, A.C., et al. (2021). Biomolecular condensation of NUP98 fusion proteins drives

leukemogenic gene expression. Nat. Struct. Mol. Biol. *28*, 190–201. https://doi.org/10.1038/s41594-020-00550-w.

17. Banani, S.F., Afeyan, L.K., Hawken, S.W., Henninger, J.E., Dall'Agnese, A., Clark, V.E., Platt, J.M., Oksuz, O., Hannett, N.M., Sagi, I., et al. (2022). Genetic variation associated with condensate dysregulation in disease. Dev. Cell *57*, 1776–1788.e8. https://doi.org/10.1016/j.devcel.2022.06.010.
18. Tripathi, S., Shirnekhi, H.K., Gorman, S.D., Chandra, B., Baggett, D.W., Park, C.-G., Somjee, R., Lang, B., Hosseini, S.M.H., Pioso, B.J., et al. (2023). Defining the condensate landscape of fusion oncoproteins. Nat. Commun. *14*, 6008. https://doi.org/10.1038/s41467-023-41655-2.
19. Yoo, H., Triandafillou, C., and Drummond, D.A. (2019). Cellular sensing by phase separation: Using the process, not just the products. J. Biol. Chem. *294*, 7151–7159. https://doi.org/10.1074/jbc.TM118.001191.
20. Mittag, T., and Pappu, R.V. (2022). A conceptual framework for understanding phase separation and addressing open questions and challenges. Mol. Cell *82*, 2201–2214. https://doi.org/10.1016/j.molcel.2022.05.018.
21. Pappu, R.V., Cohen, S.R., Dar, F., Farag, M., and Kar, M. (2023). Phase Transitions of Associative Biomacromolecules. Chem. Rev. *123*, 8945–8987. https://doi.org/10.1021/acs.chemrev.2c00814.
22. Riback, J.A., Zhu, L., Ferrolino, M.C., Tolbert, M., Mitrea, D.M., Sanders, D.W., Wei, M.-T., Kriwacki, R.W., and Brangwynne, C.P. (2020). Composition-dependent thermodynamics of intracellular phase separation. Nature *581*, 209–214. https://doi.org/10.1038/s41586-020-2256-2.
23. Li, P., Banjade, S., Cheng, H.-C., Kim, S., Chen, B., Guo, L., Llaguno, M., Hollingsworth, J.V., King, D.S., Banani, S.F., et al. (2012). Phase transitions in the assembly of multivalent signalling proteins. Nature *483*, 336–340. https://doi.org/10.1038/nature10879.
24. Sanders, D.W., Kedersha, N., Lee, D.S.W., Strom, A.R., Drake, V., Riback, J.A., Bracha, D., Eeftens, J.M., Iwanicki, A., Wang, A., et al. (2020). Competing Protein-RNA Interaction Networks Control Multiphase Intracellular Organization. Cell *181*, 306–324.e28. https://doi.org/10.1016/j.cell.2020.03.050.
25. Mitrea, D.M., Grace, C.R., Buljan, M., Yun, M.-K., Pytel, N.J., Satumba, J., Nourse, A., Park, C.-G., Madan Babu, M., White, S.W., et al. (2014). Structural polymorphism in the N-terminal oligomerization domain of NPM1. Proc. Natl. Acad. Sci. USA. *111*, 4466–4471. https://doi.org/10.1073/pnas.1321007111.
26. Mitrea, D.M., Cika, J.A., Stanley, C.B., Nourse, A., Onuchic, P.L., Banerjee, P.R., Phillips, A.H., Park, C.G., Deniz, A.A., and Kriwacki, R.W. (2018). Self-interaction of NPM1 modulates multiple mechanisms of liquid-liquid phase separation. Nat. Commun. *9*, 842. https://doi.org/10.1038/s41467-018-03255-3.
27. Falini, B., Mecucci, C., Tiacci, E., Alcalay, M., Rosati, R., Pasqualucci, L., La Starza, R., Diverio, D., Colombo, E., Santucci, A., et al. (2005). Cytoplasmic nucleophosmin in acute myelogenous leukemia with a normal karyotype. N. Engl. J. Med. *352*, 254–266. https://doi.org/10.1056/NEJMoa041974.
28. Schlenk, R.F., Döhner, K., Krauter, J., Fröhling, S., Corbacioglu, A., Bullinger, L., Habdank, M., Späth, D., Morgan, M., Benner, A., et al. (2008). Mutations and treatment outcome in cytogenetically normal acute myeloid leukemia. N. Engl. J. Med. *358*, 1909–1918. https://doi.org/10.1056/NEJMoa074306.
29. Bolli, N., Nicoletti, I., De Marco, M.F., Bigerna, B., Pucciarini, A., Mannucci, R., Martelli, M.P., Liso, A., Mecucci, C., Fabbiano, F., et al. (2007). Born to be exported: COOH-terminal nuclear export signals of different strength ensure cytoplasmic accumulation of nucleophosmin leukemic mutants. Cancer Res. *67*, 6230–6237. https://doi.org/10.1158/0008-5472.CAN-07-0273.
30. Grummitt, C.G., Townsley, F.M., Johnson, C.M., Warren, A.J., and Bycroft, M. (2008). Structural consequences of nucleophosmin mutations in acute myeloid leukemia. J. Biol. Chem. *283*, 23326–23332. https://doi.org/10.1074/jbc.M801706200.
31. Falini, B., Bolli, N., Shan, J., Martelli, M.P., Liso, A., Pucciarini, A., Bigerna, B., Pasqualucci, L., Mannucci, R., Rosati, R., et al. (2006). Both carboxy-terminus NES motif and mutated tryptophan(s) are crucial for aberrant nuclear export of nucleophosmin leukemic mutants in NPMc+ AML. Blood *107*, 4514–4523. https://doi.org/10.1182/blood-2005-11-4745.
32. Azmi, A.S., Uddin, M.H., and Mohammad, R.M. (2021). The nuclear export protein XPO1 — from biology to targeted therapy. Nat. Rev. Clin. Oncol. *18*, 152–169. https://doi.org/10.1038/s41571-020-00442-4.
33. Alcalay, M., Tiacci, E., Bergomas, R., Bigerna, B., Venturini, E., Minardi, S.P., Meani, N., Diverio, D., Bernard, L., Tizzoni, L., et al. (2005). Acute myeloid leukemia bearing cytoplasmic nucleophosmin (NPMc+ AML) shows a distinct gene expression profile characterized by up-regulation of genes involved in stem-cell maintenance. Blood *106*, 899–902. https://doi.org/10.1182/blood-2005-02-0560.
34. Spencer, D.H., Young, M.A., Lamprecht, T.L., Helton, N.M., Fulton, R., O'Laughlin, M., Fronick, C., Magrini, V., Demeter, R.T., Miller, C.A., et al. (2015). Epigenomic analysis of the HOX gene loci reveals mechanisms that may control canonical expression patterns in AML and normal hematopoietic cells. Leukemia *29*, 1279–1289. https://doi.org/10.1038/leu.2015.6.
35. Brunetti, L., Gundry, M.C., Sorcini, D., Guzman, A.G., Huang, Y.H., Ramabadran, R., Gionfriddo, I., Mezzasoma, F., Milano, F., Nabet, B., et al. (2018). Mutant NPM1 Maintains the Leukemic State through HOX Expression. Cancer Cell *34*, 499–512.e9. https://doi.org/10.1016/j.ccell.2018.08.005.
36. Uckelmann, H.J., Haarer, E.L., Takeda, R., Wong, E.M., Hatton, C., Marinaccio, C., Perner, F., Rajput, M., Antonissen, N.J.C., Wen, Y., et al. (2023). Mutant NPM1 Directly Regulates Oncogenic Transcription in Acute Myeloid Leukemia. Cancer Discov. *13*, 746–765. https://doi.org/10.1158/2159-8290.CD-22-0366.
37. Wang, X.Q.D., Fan, D., Han, Q., Liu, Y., Miao, H., Wang, X., Li, Q., Chen, D., Gore, H., Himadewi, P., et al. (2023). Mutant NPM1 Hijacks Transcriptional Hubs to Maintain Pathogenic Gene Programs in Acute Myeloid Leukemia. Cancer Discov. *13*, 724–745. https://doi.org/10.1158/2159-8290.CD-22-0424.
38. Falini, B. (2023). NPM1-mutated acute myeloid leukemia: New pathogenetic and therapeutic insights and open questions. Am. J. Hematol. *98*, 1452–1464. https://doi.org/10.1002/ajh.26989.
39. Falini, B., Brunetti, L., Sportoletti, P., and Martelli, M.P. (2020). NPM1-mutated acute myeloid leukemia: from bench to bedside. Blood *136*, 1707–1721. https://doi.org/10.1182/blood.2019004226.
40. Heikamp, E.B., Henrich, J.A., Perner, F., Wong, E.M., Hatton, C., Wen, Y., Barwe, S.P., Gopalakrishnapillai, A., Xu, H., Uckelmann, H.J., et al. (2022). The menin-MLL1 interaction is a molecular dependency in NUP98-rearranged AML. Blood *139*, 894–906. https://doi.org/10.1182/blood.2021012806.
41. Issa, G.C., Aldoss, I., DiPersio, J., Cuglievan, B., Stone, R., Arellano, M., Thirman, M.J., Patel, M.R., Dickens, D.S., Shenoy, S., et al. (2023). The menin inhibitor revumenib in KMT2A-rearranged or NPM1-mutant leukaemia. Nature *615*, 920–924. https://doi.org/10.1038/s41586-023-05812-3.
42. Uckelmann, H.J., Kim, S.M., Wong, E.M., Hatton, C., Giovinazzo, H., Gadrey, J.Y., Krivtsov, A.V., Rücker, F.G., Döhner, K., Mcgeehan, G.M., et al. (2020). Therapeutic targeting of preleukemia cells in a mouse model of NPM1 mutant acute myeloid leukemia. Science *367*, 586–590. https://doi.org/10.1126/science.aax5863.
43. Mendes, A., Jühlen, R., Martinelli, V., and Fahrenkrog, B. (2020). Targeted CRM1-inhibition perturbs leukemogenic NUP214 fusion proteins and exerts anti-cancer effects in leukemia cell lines with NUP214 rearrangements. Oncotarget *11*, 3371–3386. https://doi.org/10.18632/oncotarget.27711.
44. Dollinger, C., Potolitsyna, E., Martin, A.G., Anand, A., Datar, G.K., Schmit, J.D., and Riback, J.A. (2025). Nanometer condensate organization in live

cells derived from partitioning measurements. Preprint at bioRxiv, 2025. 02.26.640428. https://doi.org/10.1101/2025.02.26.640428.

45. Hernandez-Verdun, D. (2011). Assembly and disassembly of the nucleolus during the cell cycle. Nucleus *2*, 189–194. https://doi.org/10.4161/nucl.2.3.16246.
46. Lafontaine, D.L.J., Riback, J.A., Bascetin, R., and Brangwynne, C.P. (2021). The nucleolus as a multiphase liquid condensate. Nat. Rev. Mol. Cell Biol. *22*, 165–182. https://doi.org/10.1038/s41580-020-0272-6.
47. Rai, A.K., Chen, J.-X., Selbach, M., and Pelkmans, L. (2018). Kinase-controlled phase transition of membraneless organelles in mitosis. Nature *559*, 211–216. https://doi.org/10.1038/s41586-018-0279-8.
48. Güttinger, S., Laurell, E., and Kutay, U. (2009). Orchestrating nuclear envelope disassembly and reassembly during mitosis. Nat. Rev. Mol. Cell Biol. *10*, 178–191. https://doi.org/10.1038/nrm2641.
49. Wu, Z., Jiang, Q., Clarke, P.R., and Zhang, C. (2013). Phosphorylation of Crm1 by CDK1-cyclin-B promotes Ran-dependent mitotic spindle assembly. J. Cell Sci. *126*, 3417–3428. https://doi.org/10.1242/jcs.126854.
50. Riback, J.A., Eeftens, J.M., Lee, D.S.W., Quinodoz, S.A., Donlic, A., Orlovsky, N., Wiesner, L., Beckers, L., Becker, L.A., Strom, A.R., et al. (2023). Viscoelasticity and advective flow of RNA underlies nucleolar form and function. Mol. Cell *83*, 3095–3107.e9. https://doi.org/10.1016/j.molcel.2023.08.006.
51. Matkar, S., Thiel, A., and Hua, X. (2013). Menin: a scaffold protein that controls gene expression and cell signaling. Trends Biochem. Sci. *38*, 394–402. https://doi.org/10.1016/j.tibs.2013.05.005.
52. Hing, Z.A., Fung, H.Y.J., Ranganathan, P., Mitchell, S., El-Gamal, D., Woyach, J.A., Williams, K., Goettl, V.M., Smith, J., Yu, X., et al. (2016). Next-generation XPO1 inhibitor shows improved efficacy and in vivo tolerability in hematological malignancies. Leukemia *30*, 2364–2372. https://doi.org/10.1038/leu.2016.136.
53. Pianigiani, G., Gagliardi, A., Mezzasoma, F., Rocchio, F., Tini, V., Bigerna, B., Sportoletti, P., Caruso, S., Marra, A., Peruzzi, S., et al. (2022). Prolonged XPO1 inhibition is essential for optimal antileukemic activity in NPM1-mutated AML. Blood Adv. *6*, 5938–5949. https://doi.org/10.1182/bloodadvances.2022007563.
54. Garzon, R., Savona, M., Baz, R., Andreeff, M., Gabrail, N., Gutierrez, M., Savoie, L., Mau-Sorensen, P.M., Wagner-Johnston, N., Yee, K., et al. (2017). A phase 1 clinical trial of single-agent selinexor in acute myeloid leukemia. Blood *129*, 3165–3174. https://doi.org/10.1182/blood-2016-11-750158.
55. Oka, M., Mura, S., Otani, M., Miyamoto, Y., Nogami, J., Maehara, K., Harada, A., Tachibana, T., Yoneda, Y., and Ohkawa, Y. (2019). Chromatin-bound CRM1 recruits SET-Nup214 and NPM1c onto HOX clusters causing aberrant HOX expression in leukemia cells. eLife *8*, e46667. https://doi.org/10.7554/eLife.46667.
56. Krivtsov, A.V., Evans, K., Gadrey, J.Y., Eschle, B.K., Hatton, C., Uckelmann, H.J., Ross, K.N., Perner, F., Olsen, S.N., Pritchard, T., et al. (2019). A Menin-MLL Inhibitor Induces Specific Chromatin Changes and Eradicates Disease in Models of MLL-Rearranged Leukemia. Cancer Cell *36*, 660–673.e11. https://doi.org/10.1016/j.ccell.2019.11.001.
57. Loberg, M.A., Bell, R.K., Goodwin, L.O., Eudy, E., Miles, L.A., SanMiguel, J.M., Young, K., Bergstrom, D.E., Levine, R.L., Schneider, R.K., et al. (2019). Sequentially inducible mouse models reveal that Npm1 mutation causes malignant transformation of Dnmt3a-mutant clonal hematopoiesis. Leukemia *33*, 1635–1649. https://doi.org/10.1038/s41375-018-0368-6.
58. Dovey, O.M., Cooper, J.L., Mupo, A., Grove, C.S., Lynn, C., Conte, N., Andrews, R.M., Pacharne, S., Tzelepis, K., Vijayabaskar, M.S., et al. (2017). Molecular synergy underlies the co-occurrence patterns and phenotype of NPM1-mutant acute myeloid leukemia. Blood *130*, 1911–1922. https://doi.org/10.1182/blood-2017-01-760595.
59. Hingorani, K., Szebeni, A., and Olson, M.O. (2000). Mapping the functional domains of nucleolar protein B23. J. Biol. Chem. *275*, 24451–24457. https://doi.org/10.1074/jbc.M003278200.
60. Michmerhuizen, N.L., Klco, J.M., and Mullighan, C.G. (2020). Mechanistic insights and potential therapeutic approaches for NUP98-rearranged hematologic malignancies. Blood *136*, 2275–2289. https://doi.org/10.1182/blood.2020007093.
61. Gough, S.M., Slape, C.I., and Aplan, P.D. (2011). NUP98 gene fusions and hematopoietic malignancies: common themes and new biologic insights. Blood *118*, 6247–6257. https://doi.org/10.1182/blood-2011-07-328880.
62. Meyer, C., Larghero, P., Almeida Lopes, B., Burmeister, T., Gröger, D., Sutton, R., Venn, N.C., Cazzaniga, G., Corral Abascal, L., Tsaur, G., et al. (2023). The KMT2A recombinome of acute leukemias in 2023. Leukemia *37*, 988–1005. https://doi.org/10.1038/s41375-023-01877-1.
63. Oka, M., Otani, M., Miyamoto, Y., Oshima, R., Adachi, J., Tomonaga, T., Asally, M., Nagaoka, Y., Tanaka, K., Toyoda, A., et al. (2023). Phase-separated nuclear bodies of nucleoporin fusions promote condensation of MLL1/CRM1 and rearrangement of 3D genome structure. Cell Rep. *42*, 112884. https://doi.org/10.1016/j.celrep.2023.112884.
64. Feric, M., Vaidya, N., Harmon, T.S., Mitrea, D.M., Zhu, L., Richardson, T.M., Kriwacki, R.W., Pappu, R.V., and Brangwynne, C.P. (2016). Coexisting Liquid Phases Underlie Nucleolar Subcompartments. Cell *165*, 1686–1697. https://doi.org/10.1016/j.cell.2016.04.047.
65. Trinkle-Mulcahy, L., and Sleeman, J.E. (2017). The Cajal body and the nucleolus: "In a relationship" or "It's complicated"? RNA Biol. *14*, 739–751. https://doi.org/10.1080/15476286.2016.1236169.
66. Gu, X., Ebrahem, Q., Mahfouz, R.Z., Hasipek, M., Enane, F., Radivoyevitch, T., Rapin, N., Przychodzen, B., Hu, Z., Balusu, R., et al. (2018). Leukemogenic nucleophosmin mutation disrupts the transcription factor hub that regulates granulomonocytic fates. J. Clin. Invest. *128*, 4260–4279. https://doi.org/10.1172/JCI97117.
67. Wang, A.J., Han, Y., Jia, N., Chen, P., and Minden, M.D. (2020). NPM1c impedes CTCF functions through cytoplasmic mislocalization in acute myeloid leukemia. Leukemia *34*, 1278–1290. https://doi.org/10.1038/s41375-019-0681-8.
68. Wu, H.-C., Rérolle, D., Berthier, C., Hleihel, R., Sakamoto, T., Quentin, S., Benhenda, S., Morganti, C., Wu, C., Conte, L., et al. (2021). Actinomycin D Targets NPM1c-Primed Mitochondria to Restore PML-Driven Senescence in AML Therapy. Cancer Discov. *11*, 3198–3213. https://doi.org/10.1158/2159-8290.CD-21-0177.
69. Gourvest, M., De Clara, E., Wu, H.-C., Touriol, C., Meggetto, F., De Thé, H., Pyronnet, S., Brousset, P., and Bousquet, M. (2021). A novel leukemic route of mutant NPM1 through nuclear import of the overexpressed long noncoding RNA LONA. Leukemia *35*, 2784–2798. https://doi.org/10.1038/s41375-021-01307-0.
70. Yang, J., Chung, C.-I., Koach, J., Liu, H., Navalkar, A., He, H., Ma, Z., Zhao, Q., Yang, X., He, L., et al. (2024). MYC phase separation selectively modulates the transcriptome. Nat. Struct. Mol. Biol. *31*, 1567–1579. https://doi.org/10.1038/s41594-024-01322-6.
71. Sumner, M.C., and Brickner, J. (2022). The Nuclear Pore Complex as a Transcription Regulator. Cold Spring Harb. Perspect. Biol. *14*, a039438. https://doi.org/10.1101/cshperspect.a039438.
72. Ranganathan, P., Yu, X., Na, C., Santhanam, R., Shacham, S., Kauffman, M., Walker, A., Klisovic, R., Blum, W., Caligiuri, M., et al. (2012). Preclinical activity of a novel CRM1 inhibitor in acute myeloid leukemia. Blood *120*, 1765–1773. https://doi.org/10.1182/blood-2012-04-423160.
73. Grisendi, S., Bernardi, R., Rossi, M., Cheng, K., Khandker, L., Manova, K., and Pandolfi, P.P. (2005). Role of nucleophosmin in embryonic development and tumorigenesis. Nature *437*, 147–153. https://doi.org/10.1038/nature03915.
74. Shlush, L.I., Zandi, S., Mitchell, A., Chen, W.C., Brandwein, J.M., Gupta, V., Kennedy, J.A., Schimmer, A.D., Schuh, A.C., Yee, K.W., et al. (2014). Identification of pre-leukaemic haematopoietic stem cells in acute leukaemia. Nature *506*, 328–333. https://doi.org/10.1038/nature13038.
75. Cancer; Genome; Atlas; Research Network, Ley, T.J., Miller, C., Ding, L., Raphael, B.J., Mungall, A.J., Robertson, A.G., Hoadley, K., Triche, T.J.,

Jr., Laird, P.W., et al. (2013). Genomic and epigenomic landscapes of adult de novo acute myeloid leukemia. N. Engl. J. Med. *368*, 2059–2074. https://doi.org/10.1056/NEJMoa1301689.

76. Yamazaki, H., Takagi, M., Kosako, H., Hirano, T., and Yoshimura, S.H. (2022). Cell cycle-specific phase separation regulated by protein charge blockiness. Nat. Cell Biol. *24*, 625–632. https://doi.org/10.1038/s41556-022-00903-1.
77. Zhou, M.-H., and Yang, Q.-M. (2014). NUP214 fusion genes in acute leukemia. Oncol. Lett. *8*, 959–962. https://doi.org/10.3892/ol.2014.2263.
78. Winters, A.C., and Bernt, K.M. (2017). MLL-Rearranged Leukemias-An Update on Science and Clinical Approaches. Front. Pediatr. *5*, 4. https://doi.org/10.3389/fped.2017.00004.
79. Alexander, T.B., and Mullighan, C.G. (2021). Molecular Biology of Childhood Leukemia. Annu. Rev. Cancer Biol. *5*, 95–117. https://doi.org/10.1146/annurev-cancerbio-043020-110055.
80. Balasubramanian, S.K., Azmi, A.S., and Maciejewski, J. (2022). Selective inhibition of nuclear export: a promising approach in the shifting treatment paradigms for hematological neoplasms. Leukemia *36*, 601–612. https://doi.org/10.1038/s41375-021-01483-z.
81. Perner, F., Stein, E.M., Wenge, D.V., Singh, S., Kim, J., Apazidis, A., Rahnamoun, H., Anand, D., Marinaccio, C., Hatton, C., et al. (2023). MEN1 mutations mediate clinical resistance to menin inhibition. Nature *615*, 913–919. https://doi.org/10.1038/s41586-023-05755-9.
82. Chen, C.-W., Zhang, L., Dutta, R., Niroula, A., Miller, P.G., Gibson, C.J., Bick, A.G., Reyes, J.M., Lee, Y.-T., Tovy, A., et al. (2023). SRCAP mutations drive clonal hematopoiesis through epigenetic and DNA repair dysregulation. Cell Stem Cell *30*, 1503–1519.e8. https://doi.org/10.1016/j.stem.2023.09.011.
83. Liu, Y., Li, Q., Song, L., Gong, C., Tang, S., Budinich, K.A., Vanderbeck, A., Mathias, K.M., Wertheim, G.B., Nguyen, S.C., et al. (2024). Condensate-promoting ENL mutation drives tumorigenesis in vivo through dynamic regulation of histone modifications and gene expression. Cancer Discov. *14*, 1522–1546. https://doi.org/10.1158/2159-8290.CD-23-0876.
84. Khoo, H.M., Meaker, G.A., and Wilkinson, A.C. (2023). Ex vivo expansion and genetic manipulation of mouse hematopoietic stem cells in polyvinyl alcohol-based cultures. J. Vis. Exp. *192*. https://doi.org/10.3791/64791.
85. Cho, N.H., Cheveralls, K.C., Brunner, A.-D., Kim, K., Michaelis, A.C., Raghavan, P., Kobayashi, H., Savy, L., Li, J.Y., Canaj, H., et al. (2022). OpenCell: Endogenous tagging for the cartography of human cellular organization. Science *375*, eabi6983. https://doi.org/10.1126/science.abi6983.
86. Liebermeister, W., Noor, E., Flamholz, A., Davidi, D., Bernhardt, J., and Milo, R. (2014). Visual account of protein investment in cellular functions. Proc. Natl. Acad. Sci. USA. *111*, 8488–8493. https://doi.org/10.1073/pnas.1314810111.
87. Pianigiani, G., Rocchio, F., Peruzzi, S., Andresen, V., Bigerna, B., Sorcini, D., Capurro, M., Gjertsen, B.T., Sportoletti, P., Di Ianni, M., et al. (2022). The absent/low expression of CD34 in NPM1-mutated AML is not related to cytoplasmic dislocation of NPM1 mutant protein. Leukemia *36*, 1931–1934. https://doi.org/10.1038/s41375-022-01593-2.
88. Chi, H.T., Vu, H.A., Iwasaki, R., Nagamura, F., Tojo, A., Watanabe, T., and Sato, Y. (2010). Detection of exon 12 type A mutation of NPM1 gene in IMS-M2 cell line. Leuk. Res. *34*, 261–262. https://doi.org/10.1016/j.leukres.2009.09.019.
89. Edelstein, A.D., Tsuchida, M.A., Amodaj, N., Pinkard, H., Vale, R.D., and Stuurman, N. (2014). Advanced methods of microscope control using μManager software. J. Biol. Methods *1*, e10. https://doi.org/10.14440/jbm.2014.36.
90. Langmead, B., and Salzberg, S.L. (2012). Fast gapped-read alignment with Bowtie 2. Nat. Methods *9*, 357–359. https://doi.org/10.1038/nmeth.1923.
91. Zhang, Y., Liu, T., Meyer, C.A., Eeckhoute, J., Johnson, D.S., Bernstein, B.E., Nusbaum, C., Myers, R.M., Brown, M., Li, W., et al. (2008). Model-based analysis of ChIP-Seq (MACS). Genome Biol. *9*, R137. https://doi.org/10.1186/gb-2008-9-9-r137.
92. Ramirez, F., Ryan, D.P., Grüning, B., Bhardwaj, V., Kilpert, F., Richter, A.S., Heyne, S., Dündar, F., and Manke, T. (2016). deepTools2: a next generation web server for deep-sequencing data analysis. Nucleic Acids Res. *44*, W160–W165. https://doi.org/10.1093/nar/gkw257.
93. Li, H., Handsaker, B., Wysoker, A., Fennell, T., Ruan, J., Homer, N., Marth, G., Abecasis, G., and Durbin, R.; 1000 Genome Project Data Processing Subgroup (2009). The Sequence Alignment/Map format and SAMtools. Bioinformatics *25*, 2078–2079. https://doi.org/10.1093/bioinformatics/btp352.
94. Chen, S., Zhou, Y., Chen, Y., and Gu, J. (2018). fastp: an ultra-fast all-in-one FASTQ preprocessor. Bioinformatics *34*, i884–i890. https://doi.org/10.1093/bioinformatics/bty560.
95. Dobin, A., Davis, C.A., Schlesinger, F., Drenkow, J., Zaleski, C., Jha, S., Batut, P., Chaisson, M., and Gingeras, T.R. (2013). STAR: ultrafast universal RNA-seq aligner. Bioinformatics *29*, 15–21. https://doi.org/10.1093/bioinformatics/bts635.
96. Love, M.I., Huber, W., and Anders, S. (2014). Moderated estimation of fold change and dispersion for RNA-seq data with DESeq2. Genome Biol. *15*, 550. https://doi.org/10.1186/s13059-014-0550-8.
97. Wu, T., Hu, E., Xu, S., Chen, M., Guo, P., Dai, Z., Feng, T., Zhou, L., Tang, W., Zhan, L., et al. (2021). clusterProfiler 4.0: A universal enrichment tool for interpreting omics data. Innovation (Camb.) *2*, 100141. https://doi.org/10.1016/j.xinn.2021.100141.
98. Karjalainen, R., Pemovska, T., Popa, M., Liu, M., Javarappa, K.K., Majumder, M.M., Yadav, B., Tamborero, D., Tang, J., Bychkov, D., et al. (2017). JAK1/2 and BCL2 inhibitors synergize to counteract bone marrow stromal cell-induced protection of AML. Blood *130*, 789–802. https://doi.org/10.1182/blood-2016-02-699363.

STAR★METHODS

KEY RESOURCES TABLE

REAGENT or RESOURCE	SOURCE	IDENTIFIER
Antibodies		
anti-CRM1 antibody (rabbit)	Bethyl Labs	Cat#A300-469A-M;RRID: AB_451004
anti-NUP98 antibody (rabbit)	Cell Signaling Technology	Cat#2598T; RRID: 2267700
anti-NUP98 antibody (mouse)	Santa Cruz B	Cat#sc-74553; RRID: AB_2299066
anti-MENIN antibody (rabbit)	Cell Signaling Technology	Cat#6891S; RRID: AB_10858215
anti-KMT2A (MLL/HRX Polyclonal Antibody) (rabbit)	Active Motif	Cat#61295; RRID: AB_2793585
anti-COILIN	Cell Signaling Technology	Cat#14168T; RRID: AB_2798410
anti-PML	Cell Signaling Technology	Cat#69789S; RRID: AB_3717697
anti-SC35	Abcam	Cat#ab11826; RRID: AB_298608
anti-TDP43	Proteintech	Cat#10782-2-AP; RRID: AB_615042
anti-NPM1c antibody (western blot)	Novus Biologicals	Cat#NB110 61646SS; RRID: AB_1109535
UBE-1-100-16 (anti-NPM1c antibody for immunostaining)	Pianigiani et al.[87]	N/A
anti-NPM1wt antibody	Novus Biologicals	Cat#NB600-1030; RRID: AB_10001674
anti-GFP antibody	Novus Biologicals	Cat#NB600-308; RRID: AB_10003058
Goat anti-Rabbit IgG (H+L) Cross-Adsorbed Secondary Antibody, Alexa Fluor™ 594	Thermo Fisher Scientific	Cat#A-11012; RRID: AB_2534079
Goat anti-Mouse IgG (H+L) Cross-Adsorbed Secondary Antibody, Alexa Fluor™ 594	Thermo Fisher Scientific	Cat#A-11005; RRID: AB_2534083
Goat anti-Mouse IgG (H+L) Highly Cross-Adsorbed Secondary Antibody, Alexa Fluor™ 488	Thermo Fisher Scientific	Cat#A-11029; RRID: AB_2534088
Goat anti-Rabbit IgG (H+L) Cross-Adsorbed Secondary Antibody, Alexa Fluor™ 488	Thermo Fisher Scientific	Cat#A-11008; RRID: AB_143165
Donkey Anti-Rabbit IgG H&L (Alexa Fluor® 647)	Abcam	Cat#ab150075; RRID: AB_2752244
Goat anti-Rabbit IgG (H+L) Cross-Adsorbed Secondary Antibody, Alexa Fluor™ 647	Thermo Fisher Scientific	Cat#A-21244; RRID: AB_2535812
anti-CD117 APC antibody, mouse	eBioscience	Cat#17-1171-83; RRID: AB_46931
anti-Mac1 PE antibody, mouse	BD Biosciences	Cat#553311; RRID: AB_394775
anti-CD4 PB antibody, mouse	eBioscience	Cat#48-0452-82; RRID: AB_1648761
anti-CD8 PB antibody, mouse	BD Biosciences	Cat#558106; RRID: AB_397029
anti-B220 PB antibody, mouse	eBioscience	Cat#48-0452-82; RRID: AB_1548761
SYTOX™ Blue Dead Cell Stain, for flow cytometry	Thermo Fisher Scientific	Cat#S34857
anti-GAPDH Rhodamine antibody	BioRad	Cat#12004168; RRID: AB_2941791
StarBright™ Blue 700 Goat Anti-Rabbit IgG	BioRad	Cat#12004161; RRID: AB_2721073
StarBright™ Blue 520 Goat Anti-Mouse IgG	BioRad	Cat#12005866; RRID: AB_2934034
anti-CD11b Pacific Blue antibody	BioLegend	Cat#101223; RRID: AB_755985
anti-H3K27me3 antibody	Cell Signaling Technology	Cat#9733S; RRID: AB_2616029
mouse IgG antibody	Abcam	Cat#ab46540; RRID: AB_2614925
anti-CD45 antibody	BD Biosciences	Cat#561864; RRID: AB_11153499
Chemicals, peptides, and recombinant proteins		
Eltanexor	Selleckhem	Cat#S8397
Selinexor	Selleckhem	Cat#S7252
VTP50469	Selleckhem	Cat#S8934

(*Continued on next page*)

Continued

REAGENT or RESOURCE	SOURCE	IDENTIFIER
MI-503	Selleckhem	Cat#S7817
dTAG-13	Tocris	Cat#6605
Normal goat serum	Thermo Fisher Scientific	Cat#50062Z
36.5-38% paraformaldehyde	Sigma-Aldrich	Cat#F8775
Triton X-100 Solution	Sigma-Aldrich	Cat#93443
Ampicillin sodium salt	Sigma-Aldrich	Cat#A5354
Poly-D-Lysine	Thermo Fisher Scientific	Cat#A3890401
SR1 (StemRegenin 1)	Selleckhem	Cat#S2858
UM729	STEMCELL Technologies	Cat#72332
Fibronectin bovine PL	Andwin Scientific	Cat#80051-634
DENARASE®, 100 kU	c-LEcta GmbH	Cat#20804-100k
Dulbecco's Modified Eagle Medium (DMEM)	Thermo Fisher Scientific	Cat#11965118
StemSpan™ SFEM	STEMCELL Technologies	Cat#09600
RPMI 1640 Medium	Thermo Fisher Scientific	Cat#11875119
Dulbecco's Phosphate-Buffered Saline	GenDepot	Cat#CA008-300
Fetal Bovine Serum	Corning	Cat#35-015-CV
L-Glutamine (200 mM)	Gibco	Cat#25030081
HEPES (1M)	Gibco	Cat#15630080
Penicillin-Streptomycin (10,000 U/mL)	Invitrogen	Cat#15140122
Quick-CIP	New England Biolabs	Cat#M0525S
NEBuilder® HiFi DNA Assembly Master Mix	New England Biolabs	Cat#E2621S
KAPA HiFI HotStart ReadyMix	Roche	Cat#7958935001
XbaI	New England Biolabs	Cat#R0145S
BamHI-HF	New England Biolabs	Cat#R3136S
SPY650-DNA dye	Cytoskeleton	Cat#SC501
HOXA9 FISH probe orange-dUTP	Empire Genomics	Cat#HOXA9-20-O-R
Lymphoprep	STEMCELL Technologies	Cat#18061
Human CD34 Microbead kit	Miltenyi Biotech	Cat#130-100-453
Human recombinant IL3	STEMCELL Technologies	Cat#78040.1
Human recombinant SCF	STEMCELL Technologies	Cat#78062.1
Human Recombinant Flt3/Flk-2 Ligand	STEMCELL Technologies	Cat#78009.1
Human recombinant TPO	STEMCELL Technologies	Cat#78210
Human recombinant SCF	STEMCELL Technologies	Cat#SC501
Mouse recombinant IL3	STEMCELL Technologies	Cat#78042.1
Mouse recombinant SCF	STEMCELL Technologies	Cat#78064.1
Cas9 protein	PNA bio	Cat#CP01-200
Poly(ethylene glycol) 6000, PEG	Sigma-Aldrich	Cat#8074911000
Tween-20	BioRad	Cat#170-6531
BSA	GenDepot	Ca#A0100-010
D5000 ScreenTape	Agilent	Cat#5067-5588
High Sensitivity D1000 ScreenTape	Agilent	Cat#5067-5584
NEB 5-alpha Competent E. coli (High Efficiency)	New England Biolabs	Cat#C2987H
UltraComp eBeads	Thermo Fisher Scientific	Cat#01-3333-42
AMPure XP beads	Beckman Coulter	Cat#A63881
Lipofectamine 3000	Thermo Fisher Scientific	Cat#L3000015
Neon™ Transfection System 10 μL Kit	Thermo Fisher Scientific	Cat#MPK1096
CD117 microbeads, mouse	Miltenyi Biotec	Cat#130-091-224
Polybrene Infection / Transfection Reagent	Millipore	Cat#TR-1003-G

(*Continued on next page*)

Continued

REAGENT or RESOURCE	SOURCE	IDENTIFIER
Polyvinyl Alcohol (PVA) (250 g)	Sigma-Aldrich	Cat#P8136-250G
DNase I, RNase-free (1 U/μL)	Thermo Fisher Scientific	Cat#EN0521
Tamoxifen	Sigma-Aldrich	Cat#T2859-1G
TRIzol	Invitrogen	Cat#15596026
EveryBlot Blocking Buffer	Bio-Rad	Cat#12010020
Halt™ Protease Inhibitor Cocktail (100X)	Thermo Fisher Scientific	Cat#78429
RIPA Lysis and Extraction Buffer	Thermo Fisher Scientific	Cat#89900
Supported Nitrocellulose Membrane	Bio-Rad	Cat#1620094
4x Laemmli Sample Buffer	Bio-Rad	Cat#1610747
Critical commercial assays		
CUTANA™ DNA Purification Kit	Epicypher	Cat#14-0050
QIAquick Gel Extraction Kit	Qiagen	Cat#28704
NEBNext® Ultra™ II DNA Library Prep Kit for Illumina	New England Biolabs	Cat#E7645
RNeasy Mini Kit (50)	Qiagen	Cat#74104
RevertAid RT Reverse Transcription Kit	Thermo Fisher Scientific	Cat#K1621
2x SYBR Green qPCR Master Mix – 5ML	Selleckhem	Cat#B21202
TruSeq® Stranded mRNA Library Prep (48 Samples)	Illumina	Cat#20020594
CUTANA™ DNA Purification Kit	Epicypher	Cat#14-0050
ProFection® Mammalian Transfection System	Promega	Cat#E1200
4–20% Mini-PROTEAN® TGX™ Precast Protein Gels, 15-well, 15 μl	Bio-Rad	Cat#4561096
Deposited data		
RNA-sequencing data	This paper	GEO #GSE306285
CUT&RUN data	This paper	GEO #GSE270833
Experimental models: Cell lines		
OCI-AML3	DSMZ	Cat#ACC-582
IMS-M2	Chi et al.[88]	N/A
HL-60	ATCC	Cat# CCL-240
LOUCY	ATCC	Cat#CRL-2629
293T	ATCC	Cat#CRL-3216
HS-5	ATCC	Cat#CRL-11882
Platinum-E (Plat-E) Retroviral Packaging Cell Line	Cell Biolabs	Cat#RV-101
Lenti-X 293T	Takara	Cat#632180
U2OS	ATCC	Cat#HTB-96
Patient xenograft model (PDX2)	Brunetti et al.[35]	N/A
Human Cord Blood Samples	MD Anderson	N/A
Human Primary AML Samples (Table S2)	MD Anderson	N/A
Experimental models: Organisms/strains		
C57BL/6-Npm1tm1Trow/J (Npm1frt-cA)	Jackson Laboratory	RRID:IMSR_JAX:033164
B6(Cg)-Dnmt3atm1Trow/J (Dnmt3afl-R878H)	Jackson Laboratory	RRID:IMSR_JAX:032289
B6.FVB-Tg(EIIa-cre)C5379Lmgd/J (E2a-Cre)	Jackson Laboratory	RRID:IMSR_JAX:003724
B6N.129S6(Cg)-Gt(ROSA)26Sortm3(CAG-flpo/ERT2)Alj/J (R26FlpoER)	Jackson Laboratory	RRID:IMSR_JAX:019016
NOD.Cg-Prkdcscid Il2rgtm1Wjl Tg(CMV-IL3, CSF2,KITLG)1Eav/MloySzJ (NSG-SGM3)	Jackson Laboratory	RRID:IMSR_JAX:013062
B6.SJL-Ptprca Pepcb/BoyJ (B6 CD45.1)	Jackson Laboratory	RRID:IMSR_JAX:002014

(*Continued on next page*)

Continued

REAGENT or RESOURCE	SOURCE	IDENTIFIER
C57BL/6J (B6 CD45.2)	Jackson Laboratory	RRID:IMSR_JAX:000664
Oligonucleotides		
Custom Primers (Table S1)	IDT	N/A
Custom sgRNAs (Table S1)	Synthego	N/A
Custom HDR templates (Table S1)	Twist Biosciences	N/A
Recombinant DNA		
pMD2.G	Addgene	Plasmid#12259
pCMV delta R8.2	Addgene	Plasmid#12263
psPAX2	Addgene	Plasmid#12260
pAM-DCA-muGFP	Addgene	Plasmid#166727
pLV-bsd-EF1A>(XbaI)NPM1c-mCherry-NES (BamHI)	VectorBuilder	Vector#VB210506-1025mvz
MSCV-Luciferase-IRES-NrasG12D	Addgene	Plasmid#60834
pMYs-IRES-GFP Retroviral Expression Vector	Cell Biolabs	Plasmid#RTV-021
NRASG12D	Addgene	Plasmid#83176
pMYs-IRES-Puro Retroviral Expression Vector	Cell Biolabs	Plasmid#RTV-022
GFP-NUP98-NSD1	This paper	N/A
GFP-KMT2A-AFF1	This paper	N/A
GFP-SET-NUP214	This paper	N/A
Software and algorithms		
FACSdiva v8.0.1	BD Biosciences	N/A
FlowJo X	BD Biosciences	https://www.flowjo.com/solutions/flowjo/downloads
Graphpad Prism 7.0	Graphpad Software	http://www.graphpad.com/
Adobe Illustrator v29.1	Adobe	N/A
Snapgene 8.1.1	Dotmatics	N/A
μManager	Edelstein et al.[89]	https://micro-manager.org
Integrated Genome Viewer	Broad Institute	https://igv.org/doc/desktop/
Bowtie2 (v2.2.8)	Langmead and Salzberg[90]	https://bowtie-bio.sourceforge.net/bowtie2/index.shtml
MACS3 (v3.0.0a6)	Zhang et al.[91]	https://github.com/macs3-project/MACS
deepTools (v3.5.1)	Ramirez et al.[92]	https://deeptools.readthedocs.io/en/develop/
SAMTools (VO.1.19)	Li et al.[93]	https://www.htslib.org
R(v4.3.2)	r-project	https://www.r-project.org
fastp(v0.22.0)	Chen et al.[94]	https://github.com/OpenGene/fastp
STAR(v2.7.10a)	Dobin et al.[95]	https://github.com/alexdobin/STAR
featureCounts(v2.0.1)	Subread	http://subread.sourceforge.net/
DESeq2(v1.42.1)	Love et al.[96]	https://doi.org/10.1186/s13059-014-0550-8
clusterProfiler(v4.11.0.002)	Wu et al.[97]	https://doi.org/10.1016/j.xinn.2021.100141
conda(v4.13.0)	Conda	https://docs.conda.io/projects/conda/en/latest/index.html
Other		
NEON Transfection System	ThermoFisher	N/A
4150 TapeStation System	Agilent Technologies	Cat#G2992AA
CFX96 Touch Real-Time PCR Detection System	Bio-Rad	Cat#1845097
VisiTech instant SIM microscope (VT-iSIM)	VisiTech International	https://visitech.co.uk/vt-isim/
Hamamatsu ORCA Quest qCMOS camera	Hamamatsu	C15550-22UP
100X oil immersion objective	Nikon	CFI60 Plan Apochromat Lambda D

(*Continued on next page*)

Continued

REAGENT or RESOURCE	SOURCE	IDENTIFIER
BD LSRFortessa	BD Biosciences	N/A
BD Aria FACS	BD Biosciences	N/A
ChemiDoc™ MP Imaging System	Bio-Rad	Cat#12003154
BD LSRII benchtop cytometer	BD Biosciences	N/A

EXPERIMENTAL MODEL AND STUDY PARTICIPANT DETAILS

Cell Culture

All human suspension cell lines (OCI-AML3, IMS-M2, HL-60, and LOUCY cells) were cultured in RPMI 1640 medium supplemented with 10% FBS, 1% penicillin/streptomycin (Pen/Strep). U2OS and HS-5 cells were cultured in DMEM supplemented with 10% FBS and 1% Pen/Strep. Patient Derived Xenograft 2 (PDX2) cells and primary CD34+ cells derived from whole human cord blood were cultured in RPMI media supplemented with 10 mM L-glutamine, 10% FBS, conditioned media from human stromal HS-5 cells as previously described.[98] Mononuclear cells from fresh cord blood samples were isolated using lymphoprep density gradient (STEMCELL Technologies), stained with CD34+ beads (Miltenyi Biotech) and purified on MACS columns (Miltenyi Biotech). CD34 + HSCs were frozen in liquid nitrogen for future use.

All cells were cultured in a humidified incubator containing 5% CO_2 at 37°C. Suspension lines were grown in T-25 flasks and passaged at a 1:6 dilution approximately every 3 days. U2OS cells were grown in 10 cm^2 dishes and passaged at a 1:10 dilution every 3-4 days with trypsin (Invitrogen). PDX2 and primary human CD34+ cells were not passaged but instead supplemented with 100 ng/μL IL-3 (STEMCELL Technologies) and TPO (STEMCELL Technologies), 50 ng/μL FLT3-L (STEMCELL Technologies), 1 μM SR1 (Selleckhem), and 1 μM UM729 (STEMCELL Technologies) for 48 hours prior to CRISPR/Cas9 experiments.

Propagation of Patient Derived Xenograft Model (PDX2)

NPM1/FLT3-mutant PDX2 cells were cultured and propagated in NSG-SGM3 mice (Jackson Laboratory) as described previously.[35] Briefly, PDX2 cells were thawed and washed twice with PBS. $5x10^6$ cells were injected into sub-lethally irradiated (2.5 Gy) female NSG-SGM3 mice via tail vein. After 3 weeks, mice were sacrificed, and bone marrow cells were stained with human anti-CD45 antibodies (BD Biosciences), and engraftment rate was assessed by flow cytometry. Cells were frozen in liquid nitrogen for future use.

Primary acute myeloid leukemia samples

Deidentified fresh peripheral blood samples from acute myeloid leukemia patients with blast count exceeding 60% were purchased from the University of Texas MD Anderson Cancer Center (MDACC) Leukemia Sample Bank (Table S2). The institutional review board approved the procedure, and all patients signed a written informed consent before sample acquisition. Sequencing results of a custom panel of 81 genes recurrently mutated in hematologic malignancies, as well as standard karyotyping results were provided by MDACC. Mononuclear cells were isolated using Lymphoprep density gradient (STEMCELL Technologies) and frozen in liquid nitrogen for future use. Cells were cultured in RPMI media supplemented with 10 mM L-glutamine, 10% FBS and conditioned media from human stromal HS-5 cells. All cells were supplemented with denarase (c-LEcta) for 1 hour after thawing for all experiments.

Mice

NSG-SGM3 mice were housed in AAALAC-accredited, specific-pathogen-free animal care facilities at Baylor College of Medicine (BCM). BCM Institutional Animal Care and Use Committees approved all procedures. For all transplants, female C57BL/6J mice (6-10 weeks) were purchased from the Jackson Laboratory and immediately used for each experiment.

Dnmt3afl-R878H, E2a-Cre, Npm1frt-cA, and R26FlpoER were purchased from the Jackson Laboratory. Dnmt3afl-R878H mice were first crossed with E2a-Cre to obtain Dnmt3aR878H/+. Npm1frt-cA mice were next crossed with R26FlpoER to obtain Npm1frt-cA/R26FlpoER. Dnmt3aR878H/+ mice were then bred with Npm1frt-cA/R26FlpoER or wild-type C57BL/6J mice (Jackson Laboratory).

CRISPR/Cas9 Genetic Engineering

Generation of Homology-directed recombination templates

Knock-in experiments were performed as previously described for AML and U2OS cell lines.[35] In brief, synthetic guide RNAs (sgRNAs) targeting the wild-type and mutant NPM1 alleles (sgNPM1wt and sgNPM1c, respectively) were purchased from Synthego (Table S1). DNA templates encoding fluorescent proteins muGFP and mCherry were purchased from Addgene and Twist Biosciences respectively (Table S1). Templates were PCR amplified with KAPA HiFi HotStart ReadyMix (Roche) and custom oligomer primers to add flanking 100-200bp homology arms, generating locus-specific homologous recombination repair templates (Table S1). PCR products were purified using AMPure XP beads (Beckman Coulter) following manufacturer's instructions. To

generate fusion proteins, stop codons were replaced with a GSG linker followed by the fluorescent-protein-coding sequence and a stop codon.

Cas9-sgRNA Pre-complexing and electroporation for endogenous labeling

All experiments were performed using the Neon Transfection System (ThermoFisher) as previously described.[35] Cells were prepared in Buffer R (ThermoFisher) according to manufacturer recommendations. 2.5 x 10^5 cells were used per reaction for AML cell lines, and 6 x 10^4 cells per reaction for U2OS cells. To obtain Cas9-sgRNA ribonucleoprotein complexes, 1 μg of Cas9 protein (PNA bio) was incubated with 1 μg of sgRNA (Synthego) for 20 minutes at room temperature. For knock-in of endogenous fluorescent labels,1 μg of homology-directed recombination template was added to each reaction. AML cell lines were electroporated at the following parameters: 1400 V, 10 ms, 3 pulses. U2OS (ATCC) cells were electroporated at the following parameters: 1350 V, 35 ms, 1 pulse.

For PDX2 and primary CD34+ cells, 2.5 x 10^5 cells were prepared in Buffer T (ThermoFisher) for each reaction, and Cas9-sgRNA complexing was performed as described above. These cells were electroporated at the following parameters: 1400 V, 10 ms, 3 pulses.

METHOD DETAILS

High-Resolution Microscopy

All imaging was performed on a Nikon Ti2E equipped with a VisiTech instant SIM microscope (VisiTech International) with a Hamamatsu ORCA Quest qCMOS camera (Hamamatsu) camera using a CFI60 Plan Apochromat Lambda D 100X oil immersion objective lens (N.A. 1.45, Nikon). Imaging conditions (i.e. laser intensity) were optimized to increase signal to noise within the dynamic range. Proteins tagged with GFP were imaged using a 488nm laser, mCherry with 561nm, and Alexa 647 with 642nm. In instances where two separate fluorophores are imaged concurrently, sequential scanning was used.

Live Cell Microscopy

All imaging was performed on glass-bottom 96-well plates (Cellvis P96-1.5H-N) or 8-well glass-bottom chamber slides (Ibidi #80826) coated with Poly-D-Lysine (Thermofisher) or fibronectin (10ng/mL) for suspension and adherent cell lines respectively. Cells were maintained in 5% CO2 at 37°C during all live imaging sessions. For live cell imaging of chromatin, SPY650-DNA dye (Cytoskeleton, Inc) was added to media at a 1000X dilution according to manufacturer instructions and cells were incubated with dye for 1 hour at 37°C before imaging.

Immunostaining of human cell lines, PDX models, and primary patient samples

96-well glass bottom plates were incubated with poly-D-lysine (ThermoFisher) at 37°C for 15 minutes. Following incubation, wells were aspirated and seeded with 1-2.5 x 10^5 cells per well. The cells were incubated at 37°C for 15 minutes to allow adherence, then fixed with 4% paraformaldehyde (Sigma-Aldrich) in PBS (GenDepot) for 10 minutes at room temperature and washed with cold PBS three times. Fixed cells were simultaneously permeabilized and blocked with 0.5% Triton-X-100 (Sigma-Aldrich), 5% normal goat serum (ThermoFisher), 2% BSA (GenDepot), 0.1% Tween-20 (BioRad) in PBS at room temperature for 1 hour. Cells were then stained with rabbit or mouse primary antibodies in working solution (5% NGS, 2% BSA, 0.1% Tween-20 in PBS at 4°C overnight. Immunostaining using anti-NPM1c antibodies was performed as previously described.[87] Cells were washed 3 times with working solution before incubation with fluorescent secondary antibodies (Goat anti-rabbit or anti-mouse IgG, Alexa-Fluor 594/488 (ThermoFisher) or Donkey Anti-Rabbit, Alexa-Fluor 647 (Abcam)) in working solution for 1 hour at room temperature. Finally, cells were washed 3 times with cold working solution, stored in PBS, and protected from light, at 4°C, until imaging.

Cut-and-run Sequencing

Cut-and-run sequencing was performed using Epicypher CUTANA CUT&RUN protocol (V2.0) as described previously.[82] 1 x 10^5 cells were harvested per replicate per sample. Primary antibodies (anti-CRM1, anti-NUP98, anti-MLL, anti-MENIN, anti-H3K27me3, and IgG) were diluted 1:100 for overnight incubation, and DNA was purified with CUTANA™ DNA Purification Kit (Epicypher) according to the manufacturer's protocol. Cut-and-run sequencing library preparation was performed using NEBNext Ultra II DNA Library Prep Kit for Illumina (New England Biolabs) according to the manufacturer's protocol. Library quality was assessed with TapeStation D5000 ScreenTape (Agilent). Libraries were then sequenced using an Illumina NovaSeq 6000 sequencer, aiming for >10 million reads per condition. Paired-end enriched DNA-sequencing reads were obtained.

Pharmacological disruption of condensate formation and composition

To induce degradation of NPM1c, OCI-AML3 degron cells were treated with 500nM dTAG-13 (Tocris) for 24hrs. NPM1c protein degradation was confirmed via western blotting, flow cytometry, and live-cell microscopy. To inhibit XPO1-NPM1c interactions, cells were treated with 100nM Eltanexor (Selleckchem) or 100nM Selinexor (Selleckchem) for 24hrs as previously described.[53] To inhibit the KMT2A-MENIN interaction, cells were treated with 300nM VTP50469 (Selleckchem) or 2.5μM MI-503 (Selleckchem). 0.05% DMSO was used as a control treatment in all relevant experiments.

Lentiviral Plasmid Generation for Truncation Screen

Custom pLV-bsd-EF1A>(XbaI)NPM1c-mCherry-NES(BamHI) lentiviral vector, herein pLV, was purchased from VectorBuilder. To generate individual plasmids for truncation screen, pLV was linearized with XbaI (NEB) and BamHI-HF (NEB), purified using QIAquick Gel Extraction Kit (Qiagen), and treated with Quick-CIP (NEB) to prevent re-ligation.

DNA oligos encoding each truncation (Twist Biosciences, Table S1) were cloned into linearized pLV through 2-fragment assembly using NEBuilder HiFi DNA Assembly Master Mix (NEB) according to manufacturer recommendations. Assembled plasmids were transformed into NEB 5-alpha competent cells (NEB) and selected on LB plates with Ampicillin (50 mg/ml) (Sigma-Aldrich) at 37°C overnight before single colony isolation, plasmid extraction and validation with whole-plasmid long-read sequencing (Plasmidsaurus).

Lentivirus Generation for Truncation Screen

6-well dishes of 80-90% confluent Lenti-X 293T cells (Takara) were transfected using Lipofectamine 3000 (Invitrogen), 1.25μg of lentiviral plasmid, 625ng of pMD2.G (Addgene), and 625ng of pCMV delta R8.2 (Addgene) packaging vectors. Media containing lentiviral particles was collected at 48h and 72h after transfection. To concentrate viral particles, viral media was incubated with 4X polyethylene glycol (32% PEG6000, 0.4M NaCl, and 0.04M 4-(2-hydroxyethyl)-1-piperazineethanesulfonic acid (HEPES)) while shaking at 4°C overnight. The solution was then centrifuged at 1500xg for 45 minutes and resuspended in RPMI supplemented with 10% FBS in 1% of the original volume. Concentrated viral aliquots were stored at -80°C.

NPM1c Truncation Screen

2.5×10^5 OCI-AML3 degron cells were seeded in 24-well plates with RPMI supplemented with 7μg/ml polybrene (Millipore) and 2.5μl of concentrated viral particles. Cells were spin infected at 1100rpm for 2 hours at room temperature and returned to the incubator overnight. 24hrs after transduction, cells were washed once with PBS and replaced with fresh media. 48hrs after transduction, cells were treated with 500nM dTAG-13 or DMSO. Cells were split 1:6 every 3 days, and fresh media with 500nM dTAG-13 or DMSO was added. Flow cytometry was performed every 2–3 days to assess mCherry expression within the population. Live cell imaging was performed at day 7 as described in STAR Methods (this paper).

Flow cytometry for myeloid differentiation markers was also performed on day 14 as described previously.[35] Briefly, cells were pelleted at 300g for 5 minutes and resuspended in 50μL flow buffer (25mM HEPES, 1mM EDTA pH 8, 3% FBS in PBS) with anti-CD11b-Pacific Blue antibodies (1:100, Biolegend). Cells were incubated at room temperature in the dark for 15 minutes and 300μL flow buffer was added. Cells were gently vortexed before pelleting. Supernatant was removed, and cells resuspended in 150μL flow buffer. All samples were covered and stored on ice until analyzed. Single color controls (cell lines and UltraComp eBeads (Thermofisher) were utilized for all flow cytometry experiments for minimal compensation. All samples were run on a BD LSRII benchtop cytometer. For RNA-sequencing analysis 2.5×10^5 OCI-AML3 degron cells were treated with 500 nM dTAG -13 for 24 hours after lentiviral transduction and mCherry-positive cells were purified with FACS (BD Aria).

Retrovirus Generation for murine HSPCs transduction

$NRAS^{G12D}$-GFP vector was constructed by cloning the mutant *NRAS* gene (encoding $NRAS^{G12D}$) from MSCV vector (Addgene) into pMYs-IRES-Puro Retroviral Expression Vector (Cell Biolabs). 100 cm^2 dishes of 70% confluent Plat-E cells were transfected using ProFection Mammalian Transfection System (Promega) with 20 μg $NRAS^{G12D}$-GFP retroviral plasmid. Media containing lentiviral particles was collected at 48h and 72h after transfection. To concentrate viral particles, conditioned media from Plat-E cells was incubated with 4X PEG while shaking at 4°C overnight. The solution was then centrifuged at 1000g for 45 minutes and resuspended in StemSpan SFEM (STEMCELL Technologies). Concentrated retroviral aliquots were stored at -80°C.

Transfection of U2OS cells

U2OS cells (ATCC) were seeded at $2x10^4$/mL in a 96-well glass-bottom dish coated with 10ng/mL fibronectin (Andwin Scientific) and placed in an incubator overnight to allow adherence. On the following day, cells were transfected with Lipofectamine 3000 (Thermofisher) according to manufacturer recommendations, and 100-300ng plasmid DNA. Media was replaced the next day, and cells were imaged 48hrs after transfection.

DNA FISH

DNA FISH protocol was adapted from Liu et al.[83] Briefly, OCI-AML3 NPM1c-muGFP cells were fixed with 4% PFA, permeabilized with Triton-X-100 and stained with anti-NUP98 antibody overnight at 4°C. After staining with the secondary antibody (anti-rabbit Alexa Fluor 647), cells were cross-linked with 2% PFA and incubated with orange *HOXA9* FISH probe (Empire Genomics) during denaturation and hybridization steps.

Ex vivo VTP50469 treatment of murine HSPCs

$Dnmt3a^{R878H/+}$/Npm1flrt-cA/$R26^{FlpoER}$ mice were administered tamoxifen to induce $R26^{FlpoER}$ recombinase expression as described.[57] After recombination, 1×10^5 hematopoietic stem and progenitor cells (HSPCs) (CD45.2) were transduced with NrasG12D-GFP retroviral particles, recovered for 48 hours in PVA-based cell culture media[84] supplemented with recombinant IL3

and SCF proteins, combined with 2 x 10^6 CD45.1 bone marrow cells and retro-orbitally injected into female recipient CD45.1 mice that received a split dose of 11-Gy (lethal dose) of gamma irradiation. Donor and recipient mice ranged from 8 to 12 weeks old. Bone marrow cells from mice with >80% GFP+ cells in the peripheral blood and bone marrow were isolated and plated at 100,000 cells/well in U-bottom non-treated 96-well plates in PVA-based culture media. Cells were treated with 300 nM VTP50469 or vehicle for 72 hours (qRT-PCR analysis) or 6 days (flow cytometry analysis).

Flow cytometry analysis

Cultured murine HSPCs were stained in HBSS (Gibco) media supplemented with 2% FBS (Corning) and 10 mM HEPES (Gibco) and Penicillin-Streptomycin (Invitrogen) with anti-CD117 APC (eBioscience), anti-Mac1 PE (BD Bioscience), anti-CD4 PB (eBioscience), anti-CD8 PB (BD Bioscience), anti-B220 PB (eBioscience) antibodies, and Sytox Blue Dead Cell Stain (Thermo Fisher Scientific). Data was acquired on a LSRFortessa flow cytometer (BD) and analyzed with FlowJo X (BD Biosciences).

qPCR analysis

1000 ng of RNA was isolated using RNeasy Mini Kit (Qiagen), treated with Dnase I (Thermofisher), and used for reverse transcription reaction using the RevertAid RT Reverse Transcription Kit (ThermoFisher). qRT-PCR reaction was performed using SYBR Green qPCR mix (Selleckhem) with the following primers: *m_meis1*: TATGTGACAATTTCTGCCACCG, AGTGGATGCCGTGTCATCAT; *m_hoxa9*: TGTCCCACGCTTGACACTC, AGCGAGCATGTAGCCAGTTG; *m_hoxa10*: CGAGTCCTAGACTCCACGC, CAGTTGGCTG CATTTTCGCC; m_b2m: CTCGGTGACCCTGGTCTTTC, GGATTTCAATGTGAGGCGGG and analyzed with CFX96 Touch Real-Time PCR Detection System (Bio-Rad).

Lentiviral and retroviral transduction of murine HSPCs

HSPCs from Dnmt3a-R878H or Dnmt3a-R878H/Npm1c were purified using anti-CD117 microbeads (Miltenyi Biotec) and 1 x 10^5 cells were plated per well in 96-well plates with PVA-based culture media. Media composition was adapted from Khoo et al.[84] Cells were transduced with either PEG-concentrated retro- (NrasG12D-IRES-GFP) or lentiviral (FL-NPM1c, dNES, mCherry) particles in the presence of 7 μg/ml of polybrene (Millipore). 48 hours after transduction the efficacy was quantified with flow cytometry, and cells were used for a competitive bone marrow transplantation (1:10 ratio with wild-type CD45.1 cells) into wild-type CD45.1 recipient female mice. The percentage of GFP or mCherry cells in the peripheral blood was monitored bi-weekly with flow cytometry.

Immunoblotting

Protein lysates were obtained by lysing cell pellets in cold RIPA buffer (Thermo Fisher Scientific) supplemented with protease inhibitor cocktail (Thermo Fisher Scientific). 15-25 μG of total protein was mixed with 1x Laemmli sample buffer (Bio-Rad) and boiled at 90°C for 10 minutes. The proteins were separated by 4-20% mini-PROTEAN TGX precast protein gels (Bio-Rad) and transferred to the nitrocellulose membranes (Bio-Rad). Membranes were blocked with EveryBlot Blocking Buffer (Bio-Rad) for 1 hour and probed with the primary antibodies, anti-GAPDH (Rhodamine, Bio-Rad), anti-NPM1wt (Novus Biologicals), anti-NPM1c (Novus Biologicals), and anti-GFP (Novus Biologicals), overnight at 4°C while shaking. Membranes were washed with TBST three times and incubated with the fluorescent secondary antibodies (StarBright™ Blue 700 Goat Anti-Rabbit IgG and StarBright™ Blue 520 Goat Anti-Mouse IgG) for 1 hour at room temperature. GAPDH was used as a loading control. After washing with TBST, membranes were scanned in three channels with the ChemiDoc MP imaging system (Bio-Rad).

RNA isolation and sequencing

Cells were FACS-isolated and lysed with TRIzol (Invitrogen) for RNA isolation according to the manufacturer's protocol. RNA-sequencing was performed with the True-Seq Stranded mRNA library preparation kit (Illumina). Quality control of all libraries was performed using a TapeStation D1000 ScreenTape (Agilent). Finally, all libraries were sequenced on an Illumina Nextseq 2000 sequencer, aiming for >20 million reads per biological replicate. Paired-end RNA-sequencing reads were obtained.

Selection and determination of fusion protein sequences

Gene fusions were identified by computational (TopHat-Fusion) analysis of transcriptome sequencing data from the Cancer Genome Atlas (TCGA) (RRID:SCR_003193). To obtain fusion proteins, the list was filtered for "in-frame" gene fusions (*i.e.*, chimeric proteins made from joining two genes that usually encode separate proteins). Three fusion oncoproteins (NUP98::NSD1, KMT2A::AFF1, and SET::NUP214) were selected for this study. Their breakpoints or junctions were prioritized based on the highest frequencies of occurrence found in TCGA: NUP98 (chr11:3744509) and NSD1 (chr5:177235821); KMT2A (chr11:118482495) and AFF1 (chr4:87089984); SET (chr9:128694042) and NUP214 (chr9:131159383).

QUANTIFICATION AND STATISTICAL ANALYSIS

Quantitative Microscopy

All imaging data was analyzed in Micro-manager using a custom-built imaging plugin adapted from AcqEngJ and NDViewer. Roughly every other day, power meter measurements were done at the focal plane to verify microscope performance and allow for day-to-day

comparison of measurements. Roughly every month, dye standards were used to calibrate the DL offset and DL to photon conversion by fitting the histogram of photon counts at lower light, produce a conversion table to reference settings, and background and flat field corrections functions (functions because it was dependent on laser intensity). Linearity of the camera was verified manually as needed. For images, background field, flat field corrections, and conversion table were applied were used. Critically during quantification of intensity within an ROIs, average values within the ROI on the image background field subtracted and the flat field were calculated separately and then divided.

Concentration of NPM1wt and NPM1c within the cell

The concentration of NPM1wt is estimated at 25μM in common microscopy cell lines.[85,86] Given the levels of NPM1wt during metaphase for U2OS and OCI-AML3 are 7.5 and 6.3 RCU, respectively, we anticipate that the levels of NPM1wt in OCI-AML3 are similar. Finally, as NPM1wt and NPM1c have similar abundance (Figure S1A), we estimate that NPM1wt and NPM1c concentrations in OCI-AML3 are roughly 5-20μM and thus in the mid micromolar range. Since C-body is enriched around 10-fold in the C-body compared to its metaphase concentration, we anticipate that NPM1c concentrations are 50-200μM in the C-body.

ROI determination in live or fixed cells

For all quantification, representative areas corresponding to dilute phases of individual cellular compartments (e.g. cytoplasm and nucleoplasm) were manually selected per cell. Representative areas of dense phase structures (e.g. nucleoli and nuclear condensates) were identified by the max intensity box within an ROI (e.g. nucleus or cell) where box is defined by a size 3 by 3 pixels (when appropriate larger sizes were used).

Quantification of brightest puncta enrichment and radial distribution function in live or fixed cells

Regions of interest (ROIs) were first selected by manually drawn polygon outlines within nuclei of cells for analysis. Individuals drawing nuclear masks were blinded to fluorescent channel under investigation for enrichment in the nucleus (e.g. only NPM1c was observed when quantifying XPO1 enrichment in nuclear puncta). Radial Distribution Function calculation was performed as previously described[50] but with flat field measurements included in the denominator of the RDF and the routine being adapted into the custom built GUI within micromanager.[89]

Fitting microscopy data

The distribution for condensates/no condensates (Figure 6) as a function of concentration was determined by finding the maximum likelihood values for the sigmoidal dependence. Partitioning values were extrapolated by fitting the dilute and dense concentrations with a hyperbola and using the instantaneous slope as the partitioning. An iterative weighting routine was used to remove outliers using a protocol adapted from Dollinger et al.[44]

Cut-and-run Sequencing Analysis

CUT-and-run Sequencing analysis was performed as previously described.[82] In brief, paired-end sequencing data were mapped to the human genome (hg19) using Bowtie2.[90] Reads from biological replicates were then merged for peak calling using MACS3.[91] Quantification of peaks was performed using Subread package, where peak regions were identified as 3kb regions centered around transcriptional start sites.

RNA Sequencing

Raw paired-end sequencing data was preprocessed using Fastp[94] to exclude: (i) read lengths < 30, (ii) low quality reads (Q<25), (iii) adapter sequences. Filtered reads were mapped to the human reference (hg38) using STAR.[95] Gene-level quantification was performed through featureCounts. Low expressed genes (<10 counts) were removed before normalizing with DESeq2.[96]

Supplemental figures

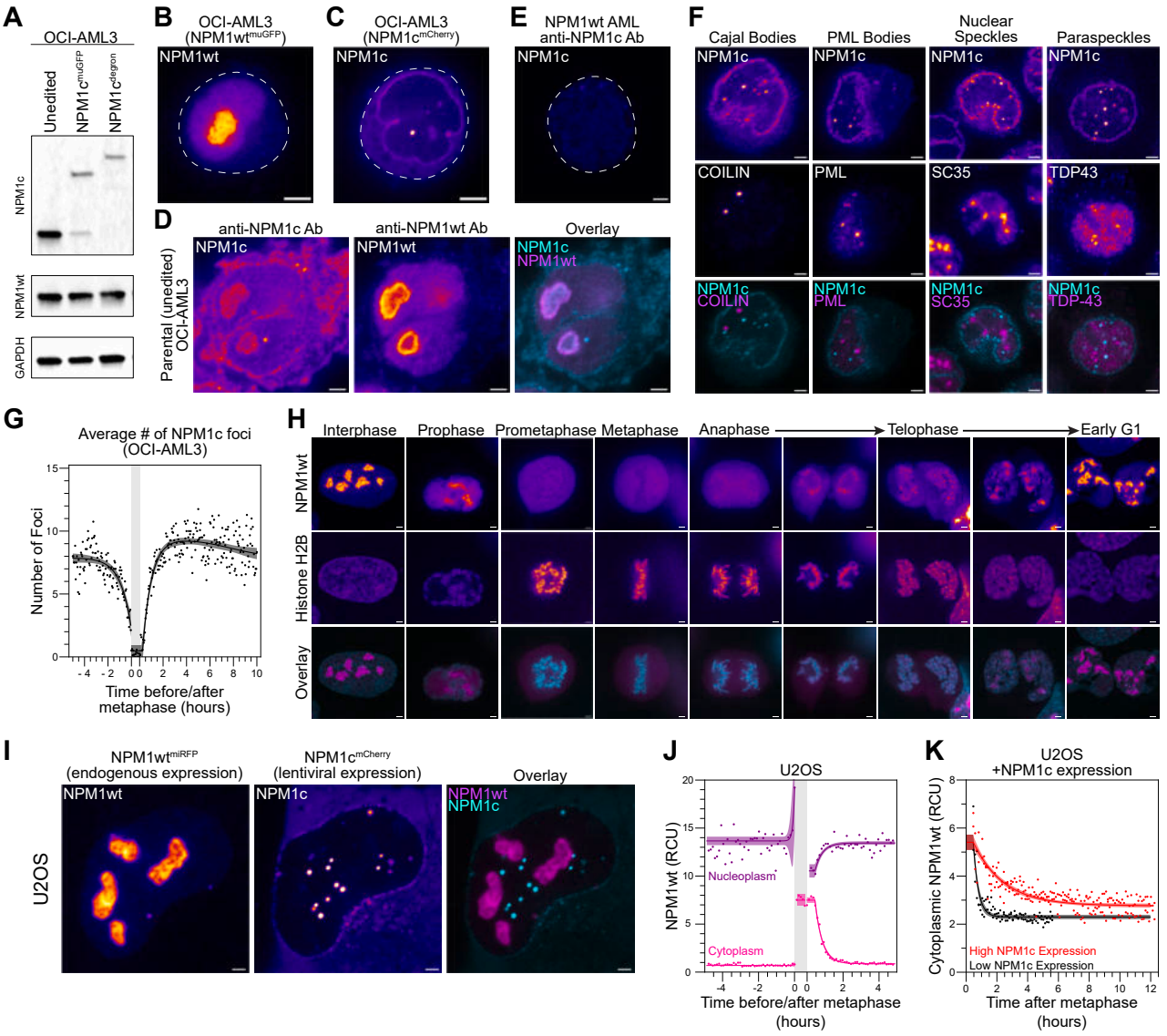

Figure S1. NPM1c forms distinct biomolecular condensates and impairs NPM1wt transit to the nucleus following cell division, related to Figure 1

(A) Immunoblotting of protein lysates from OCI-AML3 cell lines with no editing (Unedited), NPM1c tagged with muGFP (NPM1c^{muGFP}), or NPM1c tagged with an inducible degrader tag (NPM1c^{degron}) with anti-NPM1c and anti-NPM1wt antibodies. GAPDH is used as an indicator of loading control.

(B and C) Live-cell imaging of CRISPR-edited OCI-AML3 cells containing endogenous C-terminal-tagged NPM1c and NPM1wt (mCherry and muGFP, respectively).

(D) Immunostaining of parental OCI-AML3 cells.

(E) Immunostaining of *NPM1*$^{wt/wt}$ mononuclear cells derived from an AML patient without *NPM1* mutation using antibodies targeting NPM1c.

(F) Immunostaining of *NPM1*$^{WT/Degron}$ OCI-AML3 cells expressing fluorescently labeled NPM1c with antibodies targeting Cajal bodies (COILIN), PML bodies (PML), nuclear speckles (SC35), and paraspeckles (TDP43).

(G) Quantification of average number of NPM1c foci from live-cell imaging data of dual-labeled OCI-AML3 cells imaged every 3 min for ~10 h (n = 10, same dataset as in Figures 1G–1J).

(H) Live-cell imaging of dual-labeled U2OS cells expressing endogenously labeled NPM1wt (mCherry) and histone H2B (muGFP). Representative images of cell cycle stages are shown here.

(I) Live-cell imaging of U2OS cells expressing endogenously labeled NPM1wt (miRFP) transduced with NPM1c (mCherry).

(J) Quantification of U2OS cells from (H) imaged every 7 min for ~10 h (n = 5).

(legend continued on next page)

(K) Quantification of U2OS cells from (I) measuring NPM1wt (miRFP) in the cytoplasm up to 12 h after the end of metaphase. Cells with high NPM1c expression are annotated in red, while cells with low NPM1c concentration are in black. Metaphase (shaded gray) is defined by the average time between the earliest visualization of prometaphase and anaphase. Time points reflecting prometaphase through anaphase have been annotated as cytoplasm. All concentrations were measured by photons in RCUs. All images are shown in Fire LUT except colocalization (cyan and magenta). White scale bars, 2 μm.

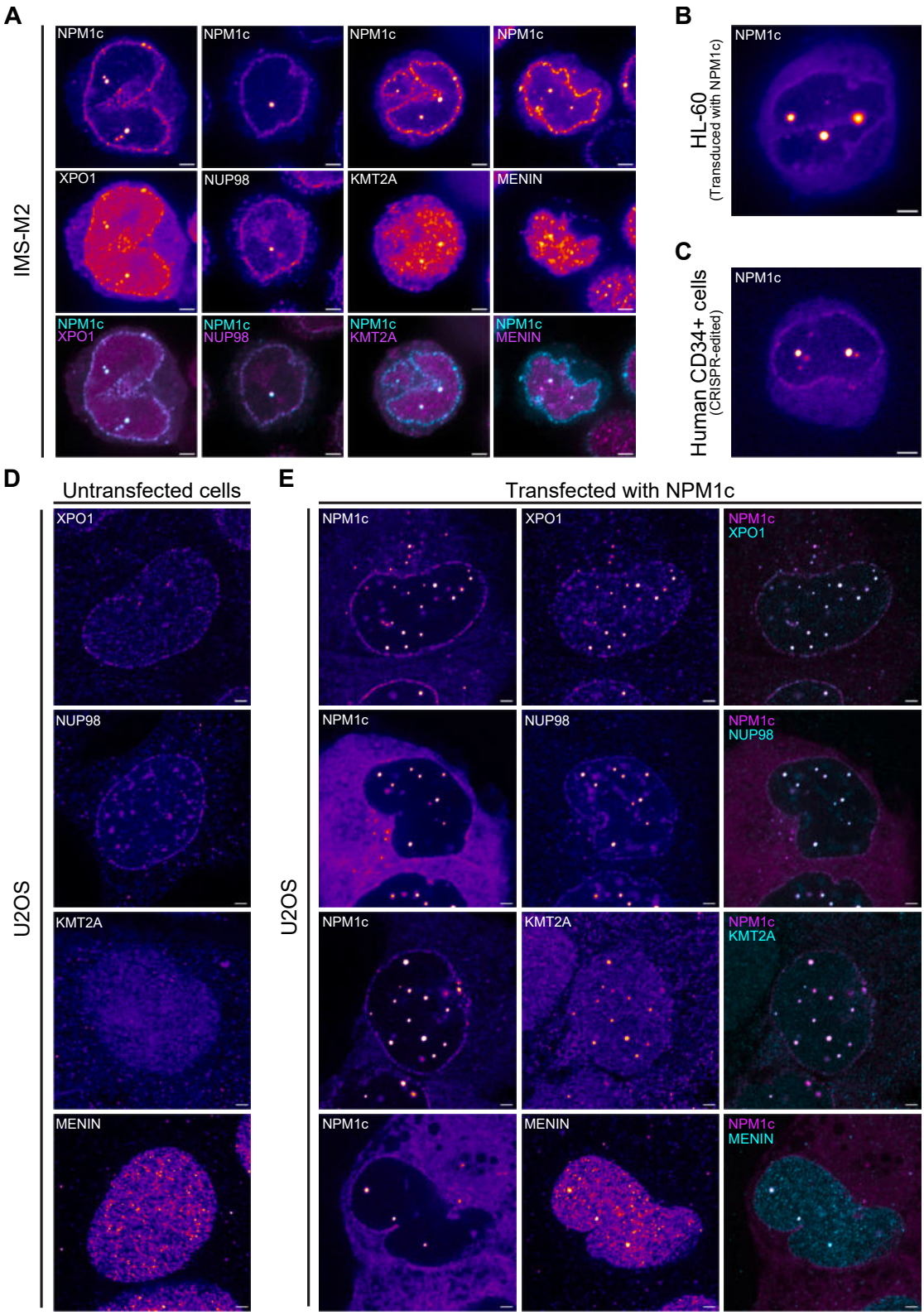

(legend on next page)

Figure S2. NPM1c is necessary and sufficient for nuclear condensate formation and punctate enrichment of C-body-associated proteins, related to Figure 2

(A) Immunostaining of *NPM1*$^{WT/Degron}$ IMS-M2 cells expressing fluorescently labeled NPM1c with antibodies targeting XPO1, NUP98, KMT2A, and MENIN.

(B) Live-cell imaging of parental HL-60 cells after viral transduction with FL-NPM1c.

(C) Live-cell imaging of human CD34^{+} cells derived from cord blood after CRISPR-editing of NPM1wt to NPM1c.

(D and E) (D) Immunostaining of parental U2OS cells and (E) parental U2OS cells transfected with NPM1c with antibodies targeting XPO1, NUP98, KMT2A, and MENIN. All images are shown in Fire LUT except colocalization (cyan and magenta). White scale bars, 2 μm.

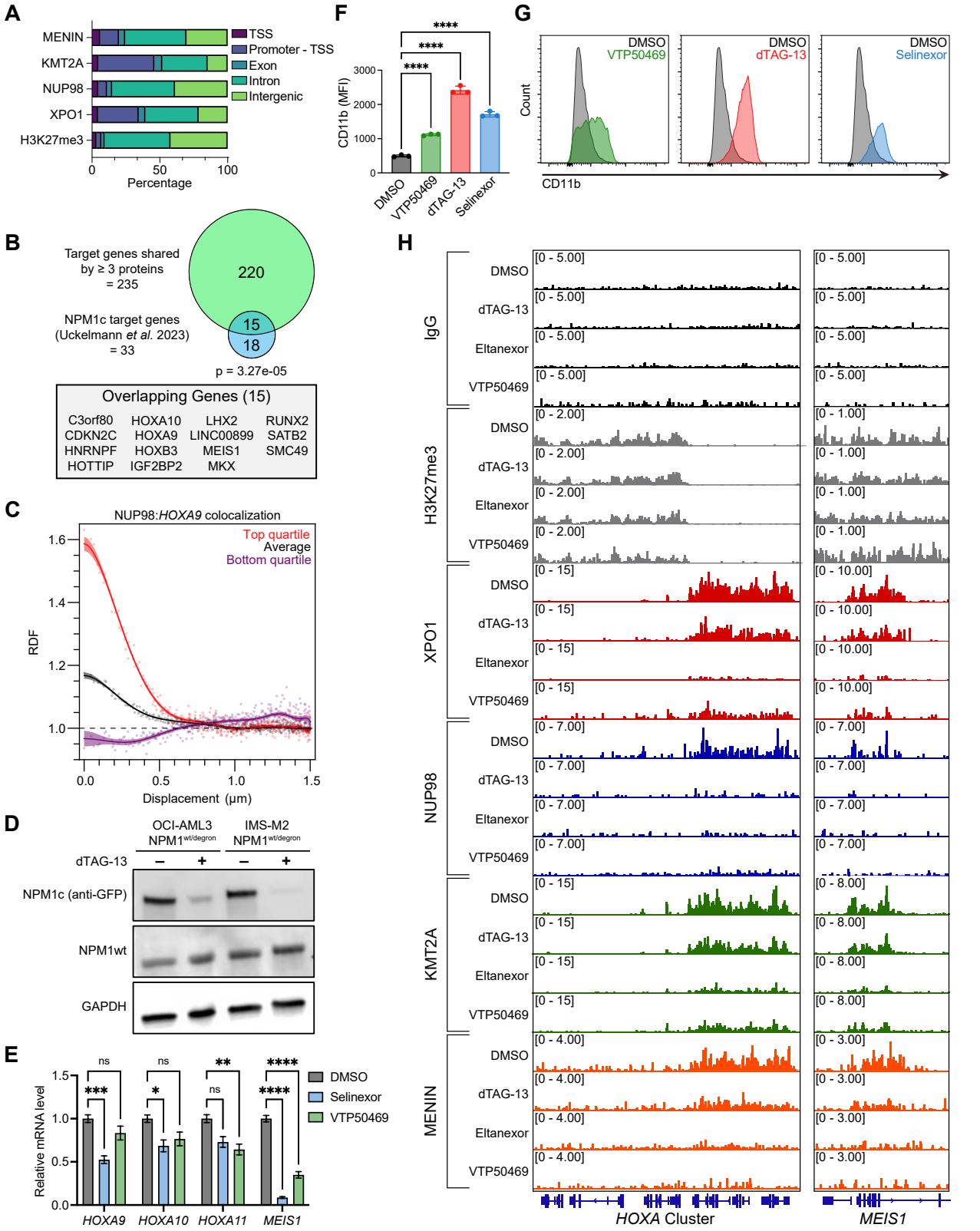

(legend on next page)

Figure S3. Condensate destabilization is associated with decreased chromatin-binding of C-body-associated proteins at key genetic loci, related to Figures 2 and 3

(A) Stacked bar plots showing distributions of CUT&RUN data from DMSO-treated *NPM1*$^{WT/Degron}$ OCI-AML3 cells, with genomic peaks annotated as transcription start sites (TSSs), promoters, exons, introns, and intergenic regions.

(B) Venn diagram of TSS-promoter peaks from DMSO-treated CUT&RUN sequencing depicting unique genes bound by at least 3 of 4 antibody targets (including XPO1, NUP98, KMT2A, and MENIN) (n = 235) and NPM1c target genes identified by ChIP-seq (n = 33[36]) and annotated table of genes found in both datasets.

(C) RDF of NUP98 and HOXA9 in top (red) and bottom (purple) quartiles in comparison to the average (n = 69).

(D) Immunoblotting analysis of protein lysates from OCI-AML3 and IMS-m2 cells treated with DMSO or dTAG for 72 h using anti-GFP, anti-NPM1wt, and anti-Gapdh-rhodamine antibodies.

(E) Relative mRNA levels of *HOXA*/*MEIS1* in OCI-AML3 cells treated with VTP50469 or Selinexor.

(F and G) (F) Mean CD11b level in OCI-AML3 cells treated with VTP50469, dTAG-13, Selinexor, or DMSO for 4 weeks, and (G) representative histograms of CD11b level.

(H) Representative integrated genome viewer (IGV) tracks (duplicates per sample) for IgG (black), H3K27me3 (gray), XPO1 (red), NUP98 (blue), KMT2A (green), and MENIN (orange) treated with DMSO, dTAG-13 (500 nM), Eltanexor (100 nM), or VTP50469 (300 nM) for 24 h. Fisher's exact test was used for statistical testing.

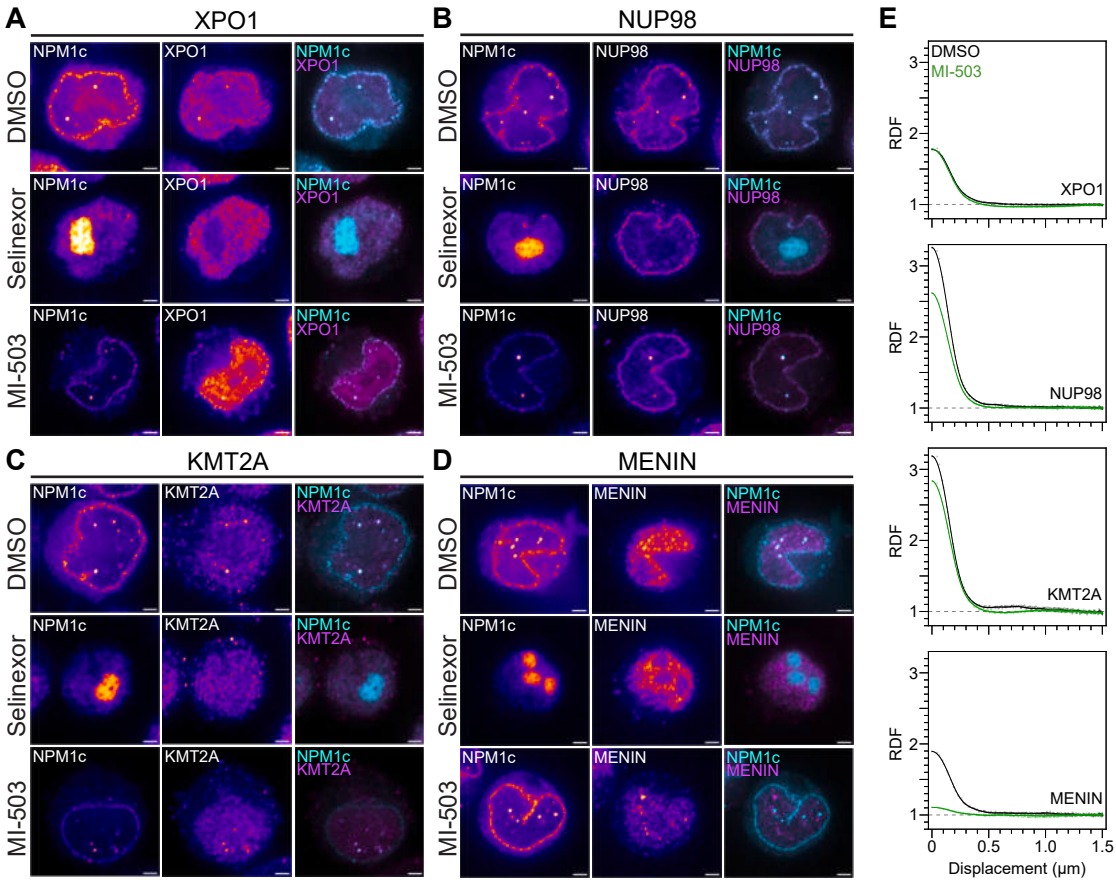

Figure S4. XPO1 and MENIN inhibition disrupt NPM1c condensate formation and composition, related to Figure 3

(A–D) Immunostaining of *NPM1*$^{WT/Degron}$ OCI-AML3 cells with antibodies targeting XPO1, NUP98, KMT2A, and MENIN after DMSO, Selinexor, or MI-503 treatments.

(E) RDF of XPO1, NUP98, KMT2A, and MENIN with DMSO or MI-503 treatment ($n = 50$). All cells were treated for 24 h prior to immunostaining (Selinexor = 100 nM, MI-503 = 2.5 μM). All images are shown in Fire LUT except colocalization (cyan and magenta). White scale bars, 2 μm. RDF data for DMSO samples is repeated from Figure 3B.

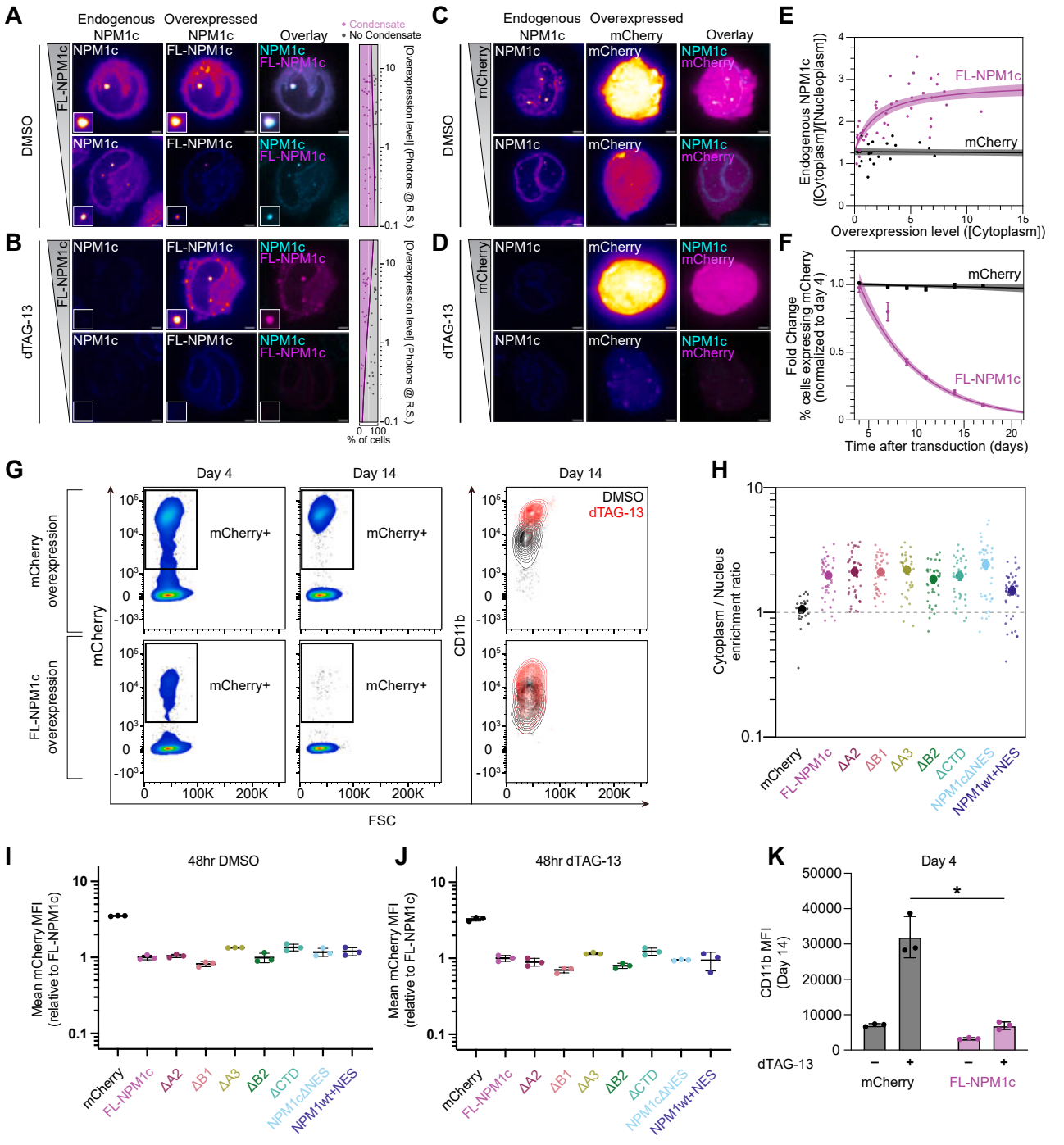

Figure S5. Overexpression of truncated NPM1c proteins and their impact on cell growth and differentiation, related to Figures 5 and 6

(A) Live-cell imaging of *NPM1*$^{WT/Degron}$ OCI-AML3 cells with stable overexpression of FL-NPM1c treated with DMSO for 24 h. Top: high FL-NPM1c expression; bottom: low FL-NPM1c expression.

(B) Live-cell imaging of *NPM1*$^{WT/Degron}$ OCI-AML3 cells treated with dTAG-13 (500 nM) for 24 h. Top: high FL-NPM1c overexpression; bottom: low FL-NPM1c expression.

(C) Live-cell imaging of *NPM1*$^{WT/Degron}$ OCI-AML3 cells with stable overexpression of mCherry treated with DMSO for 24 h. Top: high mCherry expression; bottom: low mCherry expression.

(D) Live-cell imaging of *NPM1*$^{WT/Degron}$ OCI-AML3 cells treated with dTAG-13 (500 nM) for 24 h. Top: high mCherry expression; bottom: low mCherry expression.

(E) Correlation of NPM1c and mCherry control overexpression and endogenous NPM1c localization ([cytoplasm/nucleoplasm]).

(F) Normalized fraction of cells with NPM1c or mCherry overexpression over 17 days as measured by flow cytometry.

(legend continued on next page)

(G) Representative flow cytometry plots depicting the gating strategy for mCherry+ and CD11b+ fluorescence. (Top) Cells expressing mCherry or (bottom) FL-NPM1c were analyzed at days 4 and 14 after viral transduction.
(H) Quantification of cytoplasm-to-nucleoplasm ratio of all NPM1c truncations. The dashed line represents a ratio of 1.00.
(I and J) (I) MFI of mCherry fluorescence via flow cytometry after 48 h of DMSO or (J) 500 nM dTAG-13 treatment, $n = 3$ biological replicates per truncation.
(K) MFI of CD11b via flow cytometry after 14 days of DMSO or 500 nM dTAG-13 treatment, $n = 3$ biological replicates per treatment and truncation. FL-NPM1c and mCherry data repeated from Figure 5. $^{*}p < 0.05$, *t* test with Welch's correction. All images are shown in Fire LUT except colocalization (cyan and magenta). White scale bars, 2 μm.

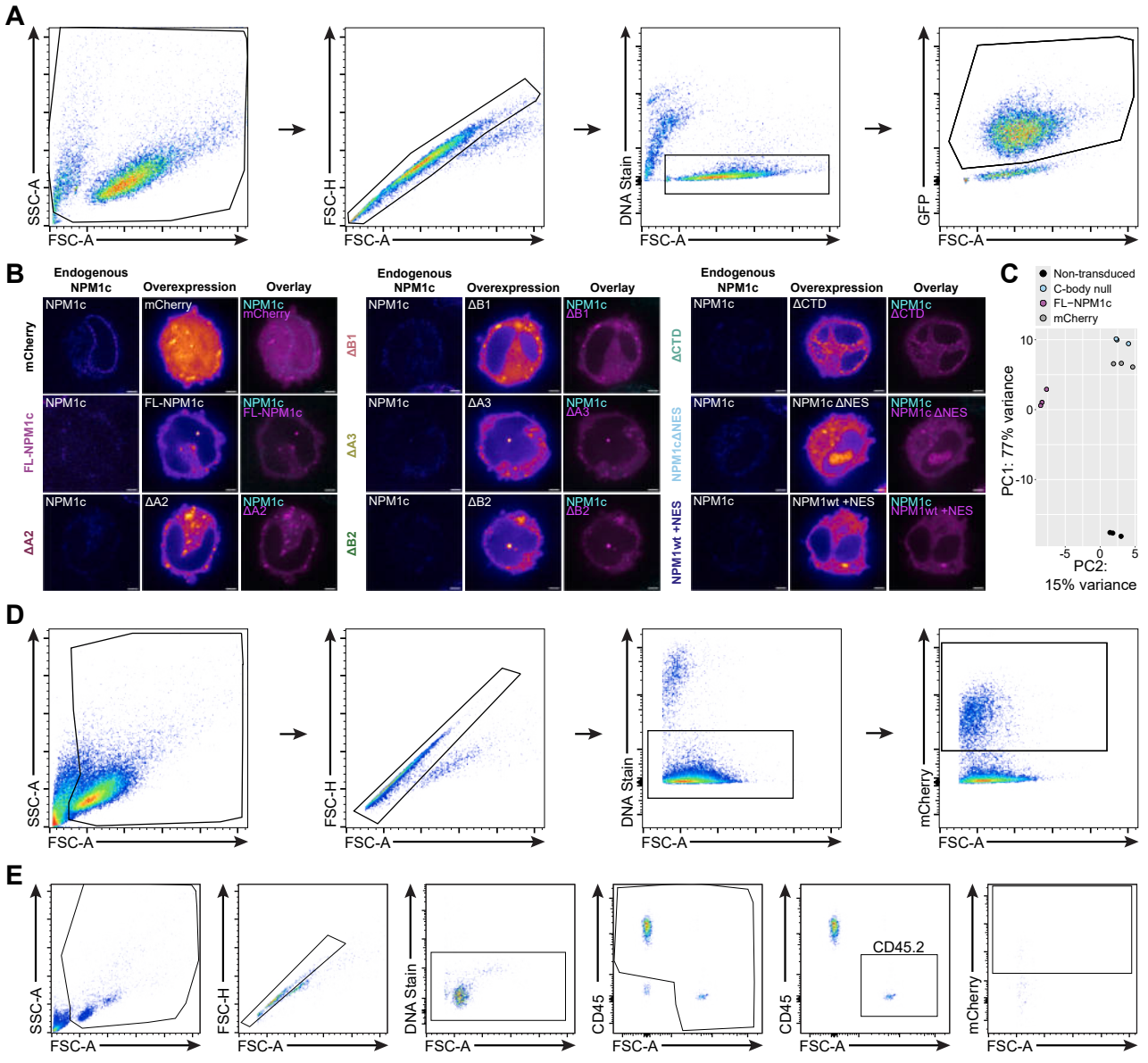

Figure S6. C-bodies in human and murine models of NPM1c AML, related to Figure 6

(A) Gating strategy for murine *Dnmt3a*$^{R878H/+}$;*Npm1*$^{cA/+}$;*Nras*$^{G12D\text{-}GFP}$ cells.

(B) Live-cell imaging of *NPM1*$^{WT/Degron}$ OCI-AML3 cells expressing NPM1c truncations treated with 500 nM dTAG-13 for 7 days.

(C) Principal-component analysis (PCA) based on variance-stabilized transcript counts of non-transduced (DMSO), C-body null, FL-NPM1c, and mCherry samples (n = 3).

(D) Gating strategy for human CD34^{+} cord blood cells expressing mCherry, FL-NPM1c, or C-body null proteins.

(E) Gating strategy for murine *Dnmt3a*$^{R878H/+}$ cells expressing mCherry, FL-NPM1c, or C-body null proteins. All images are shown in Fire LUT except colocalization (cyan and magenta). White scale bars, 2 μm.

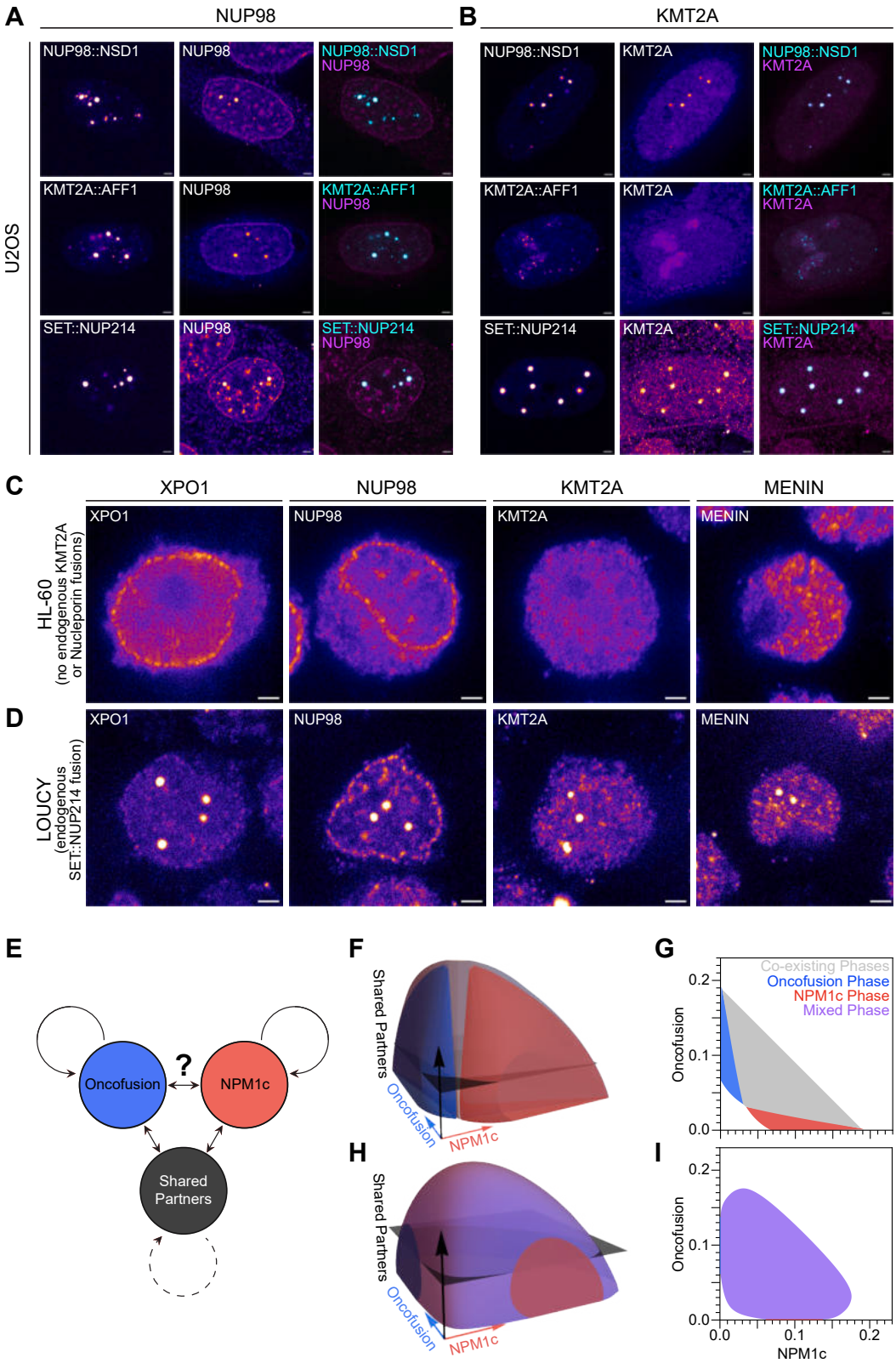

(legend on next page)

Figure S7. Oncofusion condensates recruit C-body-associated proteins and *in silico* validation of the miscibility assay, related to Figure 7

(A and B) (A) Immunostaining of U2OS cells expressing oncofusion proteins with antibodies targeting NUP98 and (B) KMT2A.

(C and D) (C) Immunostaining of parental HL-60 cells and (D) LOUCY cells with antibodies targeting XPO1, NUP98, KMT2A, and MENIN.

(E) Schematic representation of 3 components and their interactions. Solid and dashed curved arrows represent a strong (χ = 0.655) and weak (χ = 0.545) tendency to undergo phase separation, respectively. Double-headed arrows indicate a favorable interaction ($\chi = -0.143$). Interaction strength between blue and red components (shown as "?") is modeled as favorable ($\chi = -0.143$) or unfavorable (χ = 0.545) in (B), (C), (D), and (E), respectively.

(F and G) (F) Three-dimensional and (G) two-dimensional phase diagrams depicting unfavorable interactions between NPM1c and oncofusion components that result in distinguishable phases.

(H and I) (H) Three-dimensional and (I) two-dimensional phase diagrams depicting favorable interactions between NPM1c and oncofusion components that result in indistinguishable phases. All images are shown in Fire LUT except colocalization (cyan and magenta). White scale bars, 2 μm.